

Simulating the dust content of galaxies: successes and failures

Ryan McKinnon^{1*}, Paul Torrey^{1,2}, Mark Vogelsberger¹, Christopher C. Hayward^{2,3,†}, and Federico Marinacci¹

¹*Department of Physics and Kavli Institute for Astrophysics and Space Research, Massachusetts Institute of Technology, Cambridge, MA 02139, USA*

²*TAPIR, California Institute of Technology, Pasadena, CA 91125, USA*

³*Harvard-Smithsonian Center for Astrophysics, 60 Garden St., Cambridge, MA 02138, USA*

Accepted ???. Received ???; in original form ???

ABSTRACT

We present full volume cosmological simulations using the moving-mesh code AREPO to study the coevolution of dust and galaxies. We extend the dust model in AREPO to include thermal sputtering of grains and investigate the evolution of the dust mass function, the cosmic distribution of dust beyond the interstellar medium, and the dependence of dust-to-stellar mass ratio on galactic properties. The simulated dust mass function is well-described by a Schechter fit and lies closest to observations at $z = 0$. The radial scaling of projected dust surface density out to distances of 10 Mpc around galaxies with magnitudes $17 < i < 21$ is similar to that seen in Sloan Digital Sky Survey data, albeit with a lower normalisation. At $z = 0$, the predicted dust density of $\Omega_{\text{dust}} \approx 1.3 \times 10^{-6}$ lies in the range of Ω_{dust} values seen in low-redshift observations. We find that dust-to-stellar mass ratio anti-correlates with stellar mass for galaxies living along the star formation main sequence. Moreover, we estimate the $850 \mu\text{m}$ number density functions for simulated galaxies and analyse the relation between dust-to-stellar flux and mass ratios at $z = 0$. At high redshift, our model fails to produce enough dust-rich galaxies, and this tension is not alleviated by adopting a top-heavy initial mass function. We do not capture a decline in Ω_{dust} from $z = 2$ to $z = 0$, which suggests that dust production mechanisms more strongly dependent on star formation may help to produce the observed number of dusty galaxies near the peak of cosmic star formation.

Key words: dust, extinction – galaxies: evolution – galaxies: ISM – methods: numerical

1 INTRODUCTION

The dust content of high-redshift galaxies provides insight into star formation and metal enrichment at early times, and the abundance of dusty, starburst galaxies at submillimetre wavelengths (Smail, Ivison & Blain 1997; Barger et al. 1998; Hughes et al. 1998; Blain et al. 1999b; Eales et al. 1999; Scott et al. 2002) has implications for theories of galaxy formation and evolution (Blain et al. 1999a; Chary & Elbaz 2001; Dunne, Eales & Edmunds 2003; Hayward et al. 2013; Casey, Narayanan & Cooray 2014). Models are challenged to explain the presence of such galaxies and the key environmental factors that contribute to their growth. Highlighting this difficulty, there are recent observations of dusty galaxies at extremely high redshift, including HFLS3 at $z = 6.34$ with dust mass $M_{\text{dust}} = 1.3 \times 10^9 M_{\odot}$ (Riechers et al. 2013), A1689-zD1 at $z = 7.5$ with $M_{\text{dust}} = 4 \times 10^7 M_{\odot}$ (Watson et al. 2015), and two gravitationally-lensed dusty sources at $z = 5.7$ (Vieira et al. 2013; Hezaveh et al. 2013; Weiß et al. 2013).

While (ultra)luminous infrared galaxies are roughly a thou-

sand times more abundant at high redshift ($z \sim 2 - 3$) than at low redshift (Chapman et al. 2005; Lagache, Puget & Dole 2005), not all high-redshift star-forming galaxies are dust-rich. A prominent example is Himiko, a $z = 6.595$ galaxy with star-formation rate (SFR) roughly $100 M_{\odot} \text{yr}^{-1}$ but very weak dust emission (Ouchi et al. 2013). The fact that some actively star-forming galaxies are dust-rich while others are dust poor motivates a closer study of high-redshift galaxies to better understand their formation.

One important statistic is the dust mass function (DMF), whose evolution in time tracks dust growth across large populations of galaxies. The DMF was first measured at low redshift as part of the SCUBA Local Universe Galaxy Survey (Dunne et al. 2000; Dunne & Eales 2001; Vlahakis, Dunne & Eales 2005). Evolution in the DMF has been studied over $0 < z < 1$ (Eales et al. 2009; Dunne et al. 2011; Clemens et al. 2013), and observations from the Herschel ATLAS (Eales et al. 2010) find that the largest galaxies at $z = 0.5$ contained roughly five times more dust than those in the local universe (Dunne et al. 2011). The DMF has been estimated for $1 < z < 5$ using observations and number counts of submillimetre galaxies, with dust-rich galaxies showing the most change compared to the present day (Dunne, Eales & Edmunds 2003). Given the correlation between bolometric luminosity or SFR

* E-mail: ryanmck@mit.edu

† Moore Prize Postdoctoral Scholar in Theoretical Astrophysics

and dust obscuration (Wang & Heckman 1996; Adelberger & Steidel 2000; Reddy et al. 2006), the evolution of the DMF is connected to changes in the luminosity function. Luminosities of star-forming, dust-obscured galaxies at high redshift have been analysed in survey data (Reddy et al. 2006; Dey et al. 2008; Magdis et al. 2012; Magnelli et al. 2012; Lo Faro et al. 2013; Sklias et al. 2014), and galaxies at $z \sim 2$ are noticeably more luminous than their local counterparts for fixed dust obscuration (Reddy et al. 2010). However, the DMF remains less studied than statistics like the galaxy stellar mass function, particularly in the high-redshift regime where observations are challenging.

To approach this problem from a theoretical perspective, a number of models have been developed to study the population of submillimetre galaxies. Many of these models employ radiative transfer to self-consistently track absorption and reradiation of stellar light by dust (e.g. using the GRASIL (Silva et al. 1998), SUNRISE (Jonsson 2006), RADISHE (Chakrabarti & Whitney 2009), or ART² (Yajima et al. 2012) codes) and to estimate submillimetre flux densities and number counts. Radiative transfer can be combined with semi-analytic models (Baugh et al. 2005; Swinbank et al. 2008) or hydrodynamical simulations of galaxies (Chakrabarti et al. 2008; Narayanan et al. 2009, 2010; Hayward et al. 2011, 2012, 2013) to investigate how various galactic properties impact submillimetre galaxies.

Such simulations have shown that flux densities in the SCUBA 850 μm (Holland et al. 1999) and AzTEC 1.1 mm (Wilson et al. 2008) bands can be well estimated from a galaxy’s SFR and dust mass (Hayward et al. 2011). This agrees with findings that dust obscuration correlates with SFR (Adelberger & Steidel 2000). Furthermore, a top-heavy initial mass function (IMF), at least in starbursts, may help to explain number counts of submillimetre galaxies and their dust content (Baugh et al. 2005; Swinbank et al. 2008; Michałowski, Watson & Hjorth 2010).

The predictive capability of such semi-analytic and radiative transfer models motivates the inclusion of dust physics directly into galaxy formation simulations where more diverse samples of galaxies can be studied and the evolution of quantities like the DMF can be traced. The direct treatment of dust in cosmological simulations of uniform volumes provides the opportunity to investigate which environmental factors most contribute to the formation of dusty, submillimetre galaxies. It also enables comparison with a variety of observations that cannot be fully tested in simulations of individual galaxies. These include the radial scaling of projected dust surface density around galaxies to distances of several Mpc (Ménard et al. 2010), the relation between SFR, stellar mass, and dust mass at low redshift and out to $z = 2.5$ (da Cunha et al. 2010; Dunne et al. 2011; Skibba et al. 2011; Bourne et al. 2012; Cortese et al. 2012; Davies et al. 2012; Rowlands et al. 2012; Smith et al. 2012; Clemens et al. 2013; Santini et al. 2014; Rémy-Ruyer et al. 2015), and estimates of the cosmic dust density parameter Ω_{dust} and its evolution (Fukugita & Peebles 2004; Driver et al. 2007; Ménard et al. 2010; Dunne et al. 2011; Fukugita 2011; De Bernardis & Cooray 2012; Ménard & Fukugita 2012; Clemens et al. 2013; Thacker et al. 2013).

In previous work (McKinnon, Torrey & Vogelsberger 2016, hereafter M16), we introduced a dust model accounting for the production of dust through stellar evolution, accretion in the interstellar medium (ISM) via collisions with gas-phase metals, and non-thermal sputtering in supernova (SN) shocks that returned dust to the gas phase, and performed zoom-in simulations of a suite of eight Milky Way-sized haloes. Here, we extend the dust model

from M16 and perform the first cosmological simulations of galaxy populations in which dust is directly treated.

This paper is organized as follows. In Section 2, we describe the inclusion of new physics into our existing galaxy formation model and detail the initial conditions used for our simulations. In Section 3, we present our results and compare with existing data, and, in Section 4, we discuss the implications of our findings in a broader context. Finally, Section 5 summarizes our results and offers an outlook on future work.

2 METHODS

We perform cosmological simulations using the moving-mesh code AREPO (Springel 2010). The simulations incorporate the galaxy formation physics described in Vogelsberger et al. (2013). Briefly, this galaxy formation model includes gravity, hydrodynamics, primordial and metal-line cooling (Wiersma, Schaye & Smith 2009), black hole growth (Sijacki et al. 2007), star formation (Springel & Hernquist 2003), stellar evolution, chemical enrichment tracking nine elements (H, He, C, N, O, Ne, Mg, Si, and Fe), and stellar and active galactic nuclei feedback. It has been used in previous cosmological simulations, including the Illustris simulation, that trace the evolution of the galaxy stellar mass function, luminosity function, mass-metallicity relation, and other quantities and shows broad agreement with observations (Vogelsberger et al. 2012; Torrey et al. 2014; Vogelsberger et al. 2014a,b; Genel et al. 2014). In addition to this galaxy formation model, we employ a modified version of the dust model from M16, which is described below and changes our treatment of dust in the circumgalactic medium (CGM).

2.1 Dust Model

The dust model in M16 accounts for dust production from aging stellar populations, grain growth, destruction in SN shocks, and the advection and transport of dust in galactic winds. Dust is injected into the ISM as stars evolve off the main sequence, with dust masses calculated using stellar nucleosynthetic yields and estimated grain condensation efficiencies. The time-scale for grain growth through collisions between gas-phase atoms and grains depends on local gas density and temperature, while the time-scale for dust destruction through SN sputtering scales inversely with the local SNe rate. Here, we also model the evolution of dust in galactic haloes. The physics of dust grains in hot gas has been studied in detail and includes sputtering, cooling, and grain-grain collisions (Ostriker & Silk 1973; Burke & Silk 1974; Salpeter 1977; Barlow 1978; Draine & Salpeter 1979b; Itoh 1989; Tielens et al. 1994; Dwek, Foster & Vancura 1996; Smith et al. 1996). Thermal sputtering allows for the erosion of dust grains by energetic atoms, and it can limit the depletion of gas-phase metals onto grains in hot parts of a galactic halo (Burke & Silk 1974; Barlow 1978; Draine & Salpeter 1979b) and possibly enrich the intergalactic medium with metals (Bianchi & Ferrara 2005). Thermal sputtering affects grain lifetimes and gas cooling in the intracluster medium (Yahil & Ostriker 1973; Dwek & Arendt 1992; McGee & Balogh 2010). Hydrogen and helium are the main sputtering agents, and predictions of thermal sputtering rates indicate that sputtering overwhelms dust growth via accretion of gas-phase atoms for $10^5 \text{ K} < T < 10^9 \text{ K}$ (Draine & Salpeter 1979b). The strength of thermal sputtering is expected to decline sharply below $T \sim 10^6 \text{ K}$ (Ostriker & Silk 1973; Barlow 1978; Draine & Salpeter 1979b; Tielens et al. 1994; Nozawa, Kozasa & Habe 2006).

We outline below the inclusion of thermal sputtering into the dust model used in M16. It is expected that other grain destruction mechanisms, like grain-grain collisions and cosmic ray-driven sputtering, are subdominant compared to non-thermal SN shocks and thermal sputtering (Barlow 1978; Draine & Salpeter 1979a,b; Jones et al. 1994). We follow thermal sputtering prescriptions as used in previous galaxy modelling (Tsai & Mathews 1995; Hirashita et al. 2015) for simplicity of implementation.

Following Equation 14 in Tsai & Mathews (1995), we estimate the sputtering rate for a grain of radius a in gas of density ρ and temperature T as

$$\frac{da}{dt} = -(3.2 \times 10^{-18} \text{ cm}^4 \text{ s}^{-1}) \left(\frac{\rho}{m_p} \right) \left[\left(\frac{T_0}{T} \right)^\omega + 1 \right]^{-1}, \quad (1)$$

where m_p is the proton mass, $\omega = 2.5$ controls the low-temperature scaling of the sputtering rate, and $T_0 = 2 \times 10^6 \text{ K}$ is the temperature above which the sputtering rate is approximately constant. This empirical fitting formula approximately captures the temperature dependence of sputtering rates derived in theoretical calculations of collisions between spherical grains and impinging gas particles, which we outline in Appendix A (Barlow 1978; Draine & Salpeter 1979b; Tielens et al. 1994). The associated sputtering time-scale for the grain is given by Equation 15 in Tsai & Mathews (1995),

$$\tau_{\text{sp}} = a \left| \frac{da}{dt} \right|^{-1} \approx (0.17 \text{ Gyr}) \left(\frac{a_{-1}}{\rho_{-27}} \right) \left[\left(\frac{T_0}{T} \right)^\omega + 1 \right], \quad (2)$$

where a_{-1} is the grain size in units of $0.1 \mu\text{m}$ and ρ_{-27} is the gas density in units of $10^{-27} \text{ g cm}^{-3}$, which corresponds to an effective number density of $n \approx 6 \times 10^{-4} \text{ cm}^{-3}$. This time-scale is similar to the approximate sputtering time-scale given in Equation 44 of Draine & Salpeter (1979b), where detailed projectile calculations were performed. Given a grain of constant internal density ρ_g and mass $m_g = 4\pi a^3 \rho_g / 3$, Equation (2) implies that mass changes according to the time-scale $|m/\dot{m}| = \tau_{\text{sp}}/3$. In our model, we track the total dust mass for five chemical species (C, O, Mg, Si, and Fe) within each gas cell, but we do not track the grain size distribution. To account for the effect of thermal sputtering on $M_{i,\text{dust}}$, the species i dust mass within each gas cell, during every time-step we calculate the dust mass loss rate

$$\left(\frac{dM_{i,\text{dust}}}{dt} \right)_{\text{sp}} = -\frac{M_{i,\text{dust}}}{\tau_{\text{sp}}/3}, \quad (3)$$

where τ_{sp} is computed using Equation (2) and the local gas density and temperature. We fix the grain radius $a = 0.1 \mu\text{m}$ as our model is not equipped to sample across a grain size distribution. This choice for a is motivated by the facts that the grain size distribution for dust produced by AGB stars is thought to peak near $0.1 \mu\text{m}$ (Groenewegen 1997; Winters et al. 1997; Yasuda & Kozasa 2012; Asano et al. 2013b) and SNe are expected to form grains with $a \gtrsim 0.01 \mu\text{m}$ (Bianchi & Schneider 2007; Nozawa et al. 2007). We show in Appendix B that our results do not strongly depend on this grain size assumption.

Combining with the dust accretion and SN-based destruction rates from Equations 4 and 5 of M16, the net rate of dust mass change is given by

$$\frac{dM_{i,\text{dust}}}{dt} = \left(1 - \frac{M_{i,\text{dust}}}{M_{i,\text{metal}}} \right) \left(\frac{M_{i,\text{dust}}}{\tau_g} \right) - \frac{M_{i,\text{dust}}}{\tau_d} - \frac{M_{i,\text{dust}}}{\tau_{\text{sp}}/3}, \quad (4)$$

where $M_{i,\text{metal}}$ is the metal mass of species i in the cell and the growth and destruction time-scales τ_g and τ_d depend on the local density, temperature, and Type II SN rate, as indicated by Equations 5 and 7 in M16. This dust mass rate is computed on a cell-by-

cell basis for every species and used to update dust masses in every time-step.

We summarize the set of parameters and quantities that characterize our fiducial dust model in Table 1. The dust model used in this work differs from that of M16 in two respects: (i) it includes thermal sputtering, and (ii) the dust growth parameters have been changed slightly to follow from Hirashita (2000), which offers a more detailed analysis of dust growth time-scales in molecular clouds. As shown in Section 3, this latter change was adopted to lessen depletion at low redshift compared to the M16 model and better match the observed DMF and cosmic dust density parameter.

2.2 Initial Conditions and Simulations

We simulate uniformly-sampled cosmological volumes of comoving side length $L = 25 h^{-1} \text{ Mpc}$ with combined gas and dark matter particle numbers of 2×128^3 , 2×256^3 , and 2×512^3 . The gravitational softening length is held constant in comoving units until $z = 1$, after which point it is fixed to the same physical value. The maximum physical gravitational softening length is $625 h^{-1} \text{ pc}$ for the run with 2×512^3 particles.

We use ΛCDM cosmological parameters from the reanalysis of Planck data (Planck Collaboration et al. 2014) by Spergel, Flauger & Hložek (2015) of $\Omega_m = 0.302$, $\Omega_b = 0.04751$, $\Omega_\Lambda = 0.698$, $\sigma_8 = 0.817$, $n_s = 0.9671$, and $H_0 = 100 h \text{ km s}^{-1} \text{ Mpc}^{-1} = 68 \text{ km s}^{-1} \text{ Mpc}^{-1}$. Initial conditions with these parameters are generated at $z = 127$ using MUSIC (Hahn & Abel 2011) and iterated forward using AREPO. We use the SUBFIND algorithm (Springel et al. 2001; Dolag et al. 2009) for identifying gravitationally-bound structure and calculating gas, stellar, and dust mass components within galaxies. Galactic quantities are computed within twice the stellar half-mass radius.

Table 2 provides details about the simulations, including softening lengths and particle resolutions. Our fiducial simulations are performed at three resolution levels and use the fiducial galaxy formation and feedback parameters from Vogelsberger et al. (2013), including the fiducial Chabrier (2003) IMF. We perform two additional simulations to explore how sensitive our results are to the dust model we use and to the choice of IMF.

First, the ‘‘M16 model’’ run uses the dust model from M16, which lacked thermal sputtering and had dust growth parameters tuned to Milky Way-sized galaxies and resulting in fairly high depletion. The dust growth parameters used in this work and outlined in Table 1 lead to weaker dust growth than in M16.

Second, the ‘‘top-heavy IMF’’ run uses fiducial dust physics but an IMF of the form $\Phi(m) \propto m^{-1.3}$, with the same lower mass limit of $0.1 M_\odot$ and upper mass limit of $100 M_\odot$ as the fiducial IMF. The $m > 1 M_\odot$ portion of the Chabrier (2003) IMF adopts the power law $\Phi(m) \propto m^{-2.3}$, and so the top-heavy IMF we experiment with increases the exponent by one and extends the power law to the full mass range. While our top-heavy IMF is independent of galaxy properties, we note that previous works have used even more top-heavy IMFs in starbursts, like $\Phi(m) \propto m^{-1}$ (Baugh et al. 2005; Swinbank et al. 2008). It is thought that a top-heavy IMF may help form large amounts of dust at high redshift. Because the stellar feedback prescription in Vogelsberger et al. (2013) is tuned to a Chabrier (2003) IMF, for our top-heavy simulation we fix the IMF-dependent quantities in the model of Springel & Hernquist (2003) to their fiducial values. To be precise, the parameters β , the mass fraction of stars with $m > 8 M_\odot$, and ϵ_{SN} , the IMF-averaged energy returned by supernovae per solar mass of stars formed, are kept at their values for a Chabrier (2003) IMF to ensure the stellar

Table 1. Summary of parameters used in various components of the full fiducial dust model. The dust condensation efficiencies that we use to compute dust produced from stellar evolution are unchanged from those given in Table 2 of M16. The dust accretion parameters, which affect the growth time-scale calculated in Equation 5 of M16, differ slightly from those used in M16 and are based on Equation 12 in Hirashita (2000).

Parameter	Value	Description
thermal sputtering		
a	0.1	grain radius, in units of [μm]
dust accretion		
ρ^{ref}	2.3×10^{-22}	reference density roughly corresponding to $n_{\text{H}} = 100 \text{ cm}^{-3}$, in units of [g cm^{-3}]
T^{ref}	50	reference temperature, in units of [K]
$\tau_{\text{g}}^{\text{ref}}$	0.4	dust growth time-scale when $T = T^{\text{ref}}$ and $\rho = \rho^{\text{ref}}$, in units of [Gyr]
SN-based destruction		
$E_{\text{SNII},51}$	1.09	energy per SN II, in units of [10^{51} erg]

Table 2. Summary of simulation parameters and resolutions used in this work. Here, N is the total particle number, including equal numbers of dark matter and gas cells to start; ϵ is the maximum physical gravitational softening length, attained at $z = 1$; m_{dm} is the dark matter resolution; and m_{gas} is the target gas mass for each cell in the (de-)refinement scheme. The last column describes the physics for each simulation. The M16 model refers to dust model used in M16, which lacked thermal sputtering and adopted dust growth parameters $\tau^{\text{ref}} = 0.2 \text{ Gyr}$, $\rho^{\text{ref}} = 2.3 \times 10^{-24} \text{ g cm}^{-3}$, and $T^{\text{ref}} = 20 \text{ K}$, leading to stronger ISM dust growth. The top-heavy IMF run uses a pure power-law IMF of the form $\Phi(m) \propto m^{-1.3}$ over the mass range from $0.1 M_{\odot}$ to $100 M_{\odot}$. It adopts fiducial dust physics.

Name	Volume [[$h^{-1} \text{ Mpc}$] ³]	N	ϵ [$h^{-1} \text{ kpc}$]	m_{dm} [$h^{-1} M_{\odot}$]	m_{gas} [$h^{-1} M_{\odot}$]	physics
L25n128	25^3	2×128^3	2.5	5.26×10^8	9.82×10^7	fiducial
L25n256	25^3	2×256^3	1.25	6.58×10^7	1.23×10^7	fiducial
L25n512	25^3	2×512^3	0.625	8.22×10^6	1.53×10^6	fiducial
M16 model	25^3	2×256^3	1.25	6.58×10^7	1.23×10^7	model used in M16 (see caption)
top-heavy IMF	25^3	2×256^3	1.25	6.58×10^7	1.23×10^7	IMF has the form $\Phi(m) \propto m^{-1.3}$

feedback model is not strongly affected by the top-heavy IMF. In theory, to keep the Springel & Hernquist (2003) model consistent with the top-heavy IMF, we would need to increase β , which would in turn affect the SN II rate and SN-driven sputtering of dust. However, such changes would affect stellar feedback and its ability to reproduce the galaxy stellar mass function, which would complicate the interpretation of our results. To summarize, the top-heavy run adopts fiducial dust physics (including thermal sputtering and the Hirashita (2000) growth time-scale parameterisation) and for mass return uses a power-law IMF of the form $\Phi(m) \propto m^{-1.3}$, but it keeps the stellar feedback routines calibrated to the fiducial IMF.

3 RESULTS

We first use our highest resolution fiducial simulation to visualize the distribution of dust and its redshift evolution. Figure 1 shows projections of gas density, gas temperature, and dust density through a slice of the full simulation volume at $z = 2, 1,$ and 0 . The dust surface density peaks in gas-rich halo centres, where the efficient production of dust by stars and short time-scales for grain-atom collisions overcome the presence of SN sputtering. Comparing different redshifts shows that the distribution of dust is rearranged through mergers, as demonstrated by the largest halo at $z = 0$. It is also clear that large filaments of cold, diffuse gas far from potential minima – and thus sources of dust formation – have essentially no dust.

Recalling the temperature dependence of the sputtering time-scale given in Equation (2), we can see in Figure 1 that several of the largest haloes at $z = 0$ have temperatures above $T \approx 10^6 \text{ K}$. At these temperatures, the thermal velocity is high enough to erode grains. Lower mass haloes witness lower temperatures where the thermal sputtering rate falls off sharply. Regardless of halo size or temperature, dust in the cool ISM is largely unaffected by thermal sputtering, and it is interesting to consider the DMF corresponding to this diverse sample of simulated galaxies.

3.1 Dust Mass Function

We plot simulated DMFs at $z = 2.5, 1.0,$ and 0.0 in Figure 2 for our fiducial runs at three different resolutions. Figure 2 also shows the DMFs for our two model variations, one using the dust model from M16 and the other using a top-heavy IMF. Dust masses are computed within twice the stellar half-mass radius. We compare with a variety of observational data (Dunne, Eales & Edmunds 2003; Vlahakis, Dunne & Eales 2005; Eales et al. 2009; Dunne et al. 2011; Clemens et al. 2013; Clark et al. 2015), although we note that high-redshift observations are limited to the massive end of the DMF. These data have been corrected to the cosmology described in Section 2.2. We also standardise the data to the dust mass absorption coefficient $\kappa(850 \mu\text{m}) = 0.77 \text{ cm}^2 \text{ g}^{-1}$ adopted in Dunne

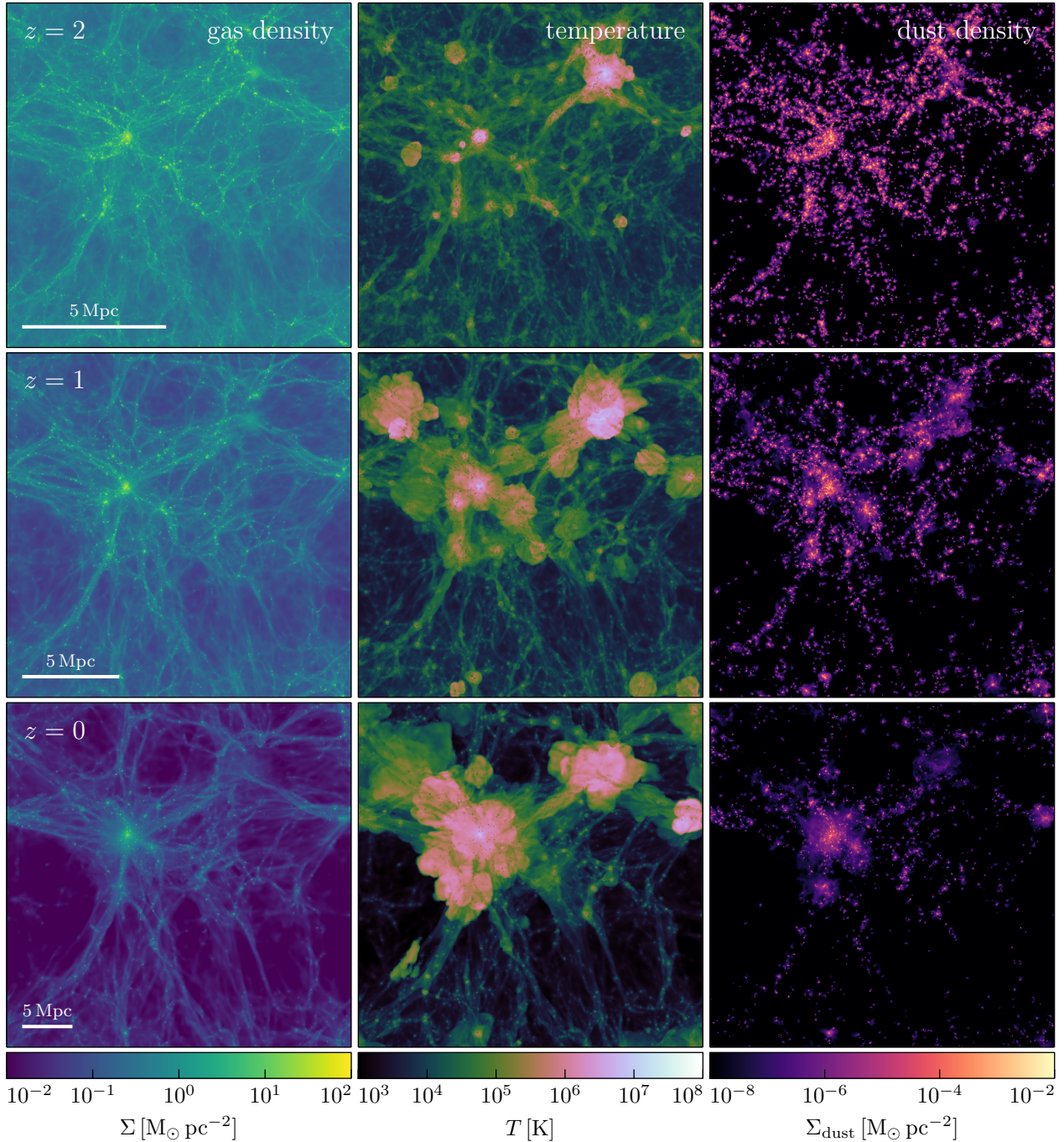


Figure 1. Projections of gas density, temperature, and dust density (left, middle, and right columns) at $z = 2, 1,$ and 0 (top, middle, and bottom rows) for the highest resolution simulation. Densities are given in physical units, and the scale bar for each redshift indicates a physical distance of 5 Mpc. Projections were performed about the centre of the simulated volume, with a height and width of $25 h^{-1}$ Mpc and a depth of $12.5 h^{-1}$ Mpc in comoving units. The distribution of dust largely traces that of gas.

et al. (2011).¹ We compare data from Dunne, Eales & Edmunds (2003) with simulated galaxies at $z = 2.5$, which is the value used in that work to compute dust masses for galaxies without spectro-

scopic redshifts. However, as noted in Section 3 of Dunne, Eales & Edmunds (2003), the estimated dust masses are largely insensitive to this choice of redshift. For the $z = 1.0$ panel, we plot data from Eales et al. (2009) over the range $0.6 < z < 1.0$. From Vlahakis, Dunne & Eales (2005), we include both the directly-measured DMF and the DMF extrapolated over a larger dust mass range using IRAS PSCz data, the latter of which is given the suffix “ex” in the legend for Figure 2.

¹ This choice of dust mass absorption coefficient means that dust mass data reported in Clemens et al. (2013), which used a value of $\kappa(850 \mu\text{m})$ smaller by roughly a factor of two, have been halved for this work.

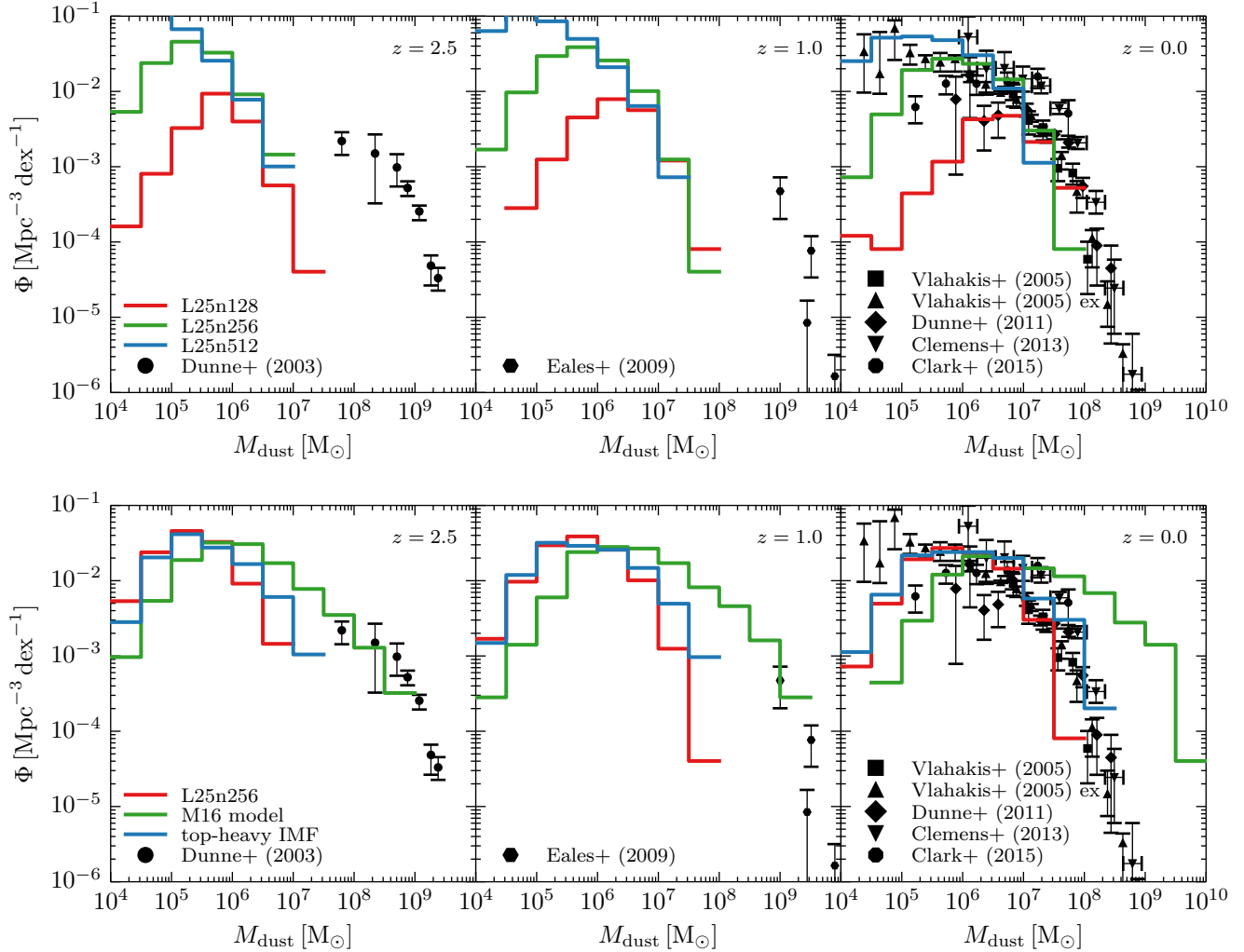


Figure 2. Simulated DMFs (coloured lines) for three resolution levels (top row) and model variations (bottom row) as compared with observations (black points) for $z = 2.5$, 1.0 , and 0.0 (left, middle, and right panels, respectively). For [Eales et al. \(2009\)](#), we plot data from $0.6 < z < 1.0$. From [Vlahakis, Dunne & Eales \(2005\)](#) we include both the directly measured DMF and the IRAS PSCz-extrapolated DMF, the latter of which has the suffix “ex” in the legend. For [Dunne et al. \(2011\)](#), we use the $0.0 < z < 0.1$ set of data and cap the uncertainty at 1 dex for two data points to improve readability. Observations have been corrected to conform to the cosmology detailed in Section 2.2. While the fiducial simulated DMFs offer a decent fit to observations at $z = 0.0$, they fail to produce an abundance of dust-rich galaxies at higher redshift.

While our fiducial model offers a reasonable fit to observed data at $z = 0.0$ down to the resolution limit, it does not reproduce the abundance of high dust mass galaxies near $z = 2.5$ and $z = 1.0$. At $z = 2.5$, the number density of simulated galaxies with $M_{\text{dust}} \approx 10^7 M_{\odot}$ is similar to that for observed galaxies with $M_{\text{dust}} \approx 10^9 M_{\odot}$. Although our simulated value of $\Phi(M_{\text{dust}} \approx 2 \times 10^7 M_{\odot})$ increases by over 1 dex from $z = 2.5$ to 1.0 , we still have difficulty producing enough dust-rich galaxies at $z = 1.0$. The nature of dust processes makes the DMF behave in a much more dynamic way than the galaxy stellar mass function, since there is a diversity of ways for dust to grow (e.g. stellar injection of grains and collisions with gas in the ISM) and be destroyed (e.g. SN shocks and thermal sputtering). This same core galaxy formation model without dust tracking had success in matching the galaxy stellar mass function’s gradual flattening at the low mass end from high to low redshift as more galaxies gain stellar mass ([Vogelsberger et al. 2013](#); [Torrey et al. 2014](#); [Vogelsberger et al. 2014a,b](#); [Genel et al. 2014](#)). However, the DMF does not evolve in

such a monotonic fashion: galaxies at $z = 2.5$ tend to be more dust-rich than at $z = 0.0$ ([Dunne, Eales & Edmunds 2003](#)), and, even from $z = 0.5$ to $z = 0.0$, galactic dust masses decline by about a factor of five ([Dunne et al. 2011](#)). It is worth noting that for mass bins of width 0.5 dex, a DMF value of $\Phi = 10^{-4} \text{Mpc}^{-3} \text{dex}^{-1}$ corresponds to roughly two galaxies in our fiducial volume. Thus, the massive ends of our DMFs are sensitive to Poissonian statistics. In Appendix C, we simulate a volume eight times as large down to $z = 2.5$ and investigate its DMF. The greater sample size provided by a larger volume does not alleviate the absence of very dusty galaxies. Furthermore, the fiducial runs do not display robust convergence as the resolution is increased. At $z = 0.0$, the DMF falls off at the high-mass end more quickly with increasing resolution. As a result, number densities associated with the L25n512 run lie above those for the L25n128 run in some mass bins, while the trend is reversed in other bins. We note in Section 3.3 that volume-averaged quantities like comoving dust density display better convergence properties.

In Figure 2, the dust model used in M16, which had a stronger dust growth mechanism and lacked thermal sputtering, differs the most from the fiducial model at $z = 0.0$ and overproduces dust-rich galaxies. This is consistent with the finding in M16 that strong dust growth can overdeplete gas-phase metals at late times. These results are largely unaffected by the inclusion of thermal sputtering since the DMFs in Figure 2 isolate dust in the fairly cool ISM. However, the M16 model does predict more dust-rich galaxies at $z = 2.5$ than the fiducial model and lies close to the Dunne, Eales & Edmunds (2003) data. A dust growth mechanism that allows for more variation among galaxies of different masses and SFRs may be needed to form dust-rich galaxies at high redshift but also avoid overproducing dust at low redshift.

Similarly, the run with a top-heavy IMF, $\Phi(m) \propto m^{-1.3}$, produces more dust than the fiducial L25n256 run at all redshifts. This is consistent with a top-heavy IMF shifting the galaxy stellar mass function towards lower masses due to shorter average stellar lifetimes. However, even this top-heavy IMF is unable to produce enough dust-rich galaxies at $z = 2.5$. This suggests that the tension between our fiducial model and high-redshift observations of massive, dusty galaxies cannot be remedied by a variation in IMF.

For the fiducial $z = 0.0$ results, we fit data from the L25n512 run with a Schechter function (Schechter 1976) of the form

$$\Phi(M_{\text{dust}}) \Delta M_{\text{dust}} = \Phi^* \left(\frac{M_{\text{dust}}}{M_{\text{dust}}^*} \right)^\alpha \exp \left(\frac{-M_{\text{dust}}}{M_{\text{dust}}^*} \right) \Delta \left(\frac{M_{\text{dust}}}{M_{\text{dust}}^*} \right) \quad (5)$$

to determine the best-fitting slope parameter α , characteristic dust mass M_{dust}^* , and normalisation factor Φ^* . We obtain $\alpha = -1.03$, $M_{\text{dust}}^* = 3.5 \times 10^6 M_\odot$, and $\Phi^* = 2.2 \times 10^{-2} \text{Mpc}^{-3} \text{dex}^{-1}$. For comparison, the best-fitting Schechter function in Dunne et al. (2011) for $0.0 < z < 0.1$ produces $\alpha = -1.01$, $M_{\text{dust}}^* = 3.83 \times 10^7 M_\odot$, and $\Phi^* = 5.87 \times 10^{-3} \text{Mpc}^{-3} \text{dex}^{-1}$. Relative to this observational data, the L25n512 run yields a similar slope parameter, and though it predicts a lower turnover mass and higher normalisation factor, Figure 16 in Dunne et al. (2011) demonstrates how these parameters are degenerate and anti-correlated.

3.2 Projected Dust Surface Density

The visualizations in Figure 1 suggest that lines of sight far from galaxies suffer little dust extinction. We can directly quantify this by considering the dust surface density in galactic haloes. One observational technique to detect dust in haloes involves cross-correlating the brightness of quasars with the position of galaxies to infer reddening from dust (Ménard et al. 2010). This correlation is used to estimate galactic reddening and infer dust surface density profiles, with the mean dust surface density following the scaling $\Sigma_{\text{dust}} \propto r^{-0.8}$. This relation has been reproduced by analytic halo models (Masaki & Yoshida 2012), and a similar technique has been used to study the distribution of dust on larger scales in galaxy clusters (McGee & Balogh 2010).

In Figure 3, we show the dust surface density profile as a function of projected radial distance in physical units around galactic centres at $z = 0.3$, averaging over all galaxies with $17 < i < 21$ to match the magnitude cut used in Ménard et al. (2010). We calculate apparent magnitudes for simulated galaxies using the procedure outlined in Section 3.1 of Torrey et al. (2014). Briefly, we use the stellar population synthesis model of Bruzual & Charlot (2003) and assign a luminosity to each star particle as a function of its age, initial stellar mass, and metallicity, and then we set each galaxy's

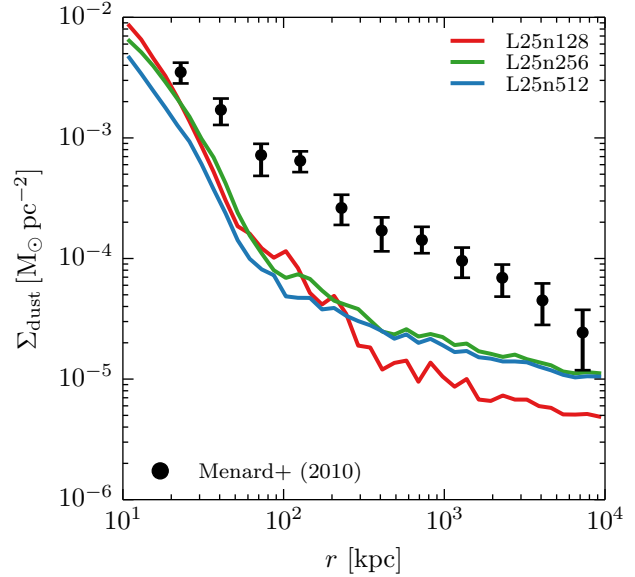


Figure 3. Dust surface density (Σ_{dust}) as a function of projected radius about galactic centres at $z = 0.3$ out to distances of 10 Mpc in physical units. For each simulation, we show the mean dust surface density profile averaged across galaxies with $17 < i < 21$, using projections along the z axis of our box to ensure random orientations. This enables comparison with observational data from Ménard et al. (2010), shown in black, where galaxy position and quasar brightness correlations are used to infer reddening and SMC-type dust is assumed. The simulated dust surface density scaling has lower normalisation than the observed result, particularly at large radii.

luminosity to be the sum of the luminosities for constituent star particles. To determine apparent magnitudes, we use the luminosity distance $D_L = 1598 \text{Mpc}$ for $z = 0.3$ in our cosmology. We perform projections for individual galaxies along the z axis of our simulated box, resulting in random orientations with respect to the projection axis. Every projection is carried out in a cylindrical volume centered on the galactic potential minimum, using a radius of 10 Mpc and a half-height of 20 Mpc. Reducing this cylinder height by a factor of two leaves the profiles in Figure 3 virtually unchanged for radii less than 1 Mpc and lowers them by about 0.2 dex at the maximum radius of 10 Mpc. The mean dust surface density profile for all galaxies in this magnitude range is the result shown in Figure 3. As noted in Ménard et al. (2010), on scales larger than the virial radius, the dust surface density profile may be influenced by dust from surrounding or overlapping galaxies.

The simulated dust surface density profiles appear well-converged out to $r \approx 50 \text{kpc}$, with the two highest-resolution runs showing slightly greater dust surface density out to Mpc scales. Compared to the observed $\Sigma_{\text{dust}} \propto r^{-0.8}$ scaling, the simulated profiles are steeper for $r < 100 \text{kpc}$ and flatter for $r > 100 \text{kpc}$. The dust surface density from our even highest resolution run still lies below the observed data, with the tension largest for large radial distances.

3.3 Cosmic Dust Density

In Figure 4, we show the comoving cosmic dust density ρ_{dust} as a function of redshift for our simulations and compare with observational data at low redshift. The observational data have been cor-

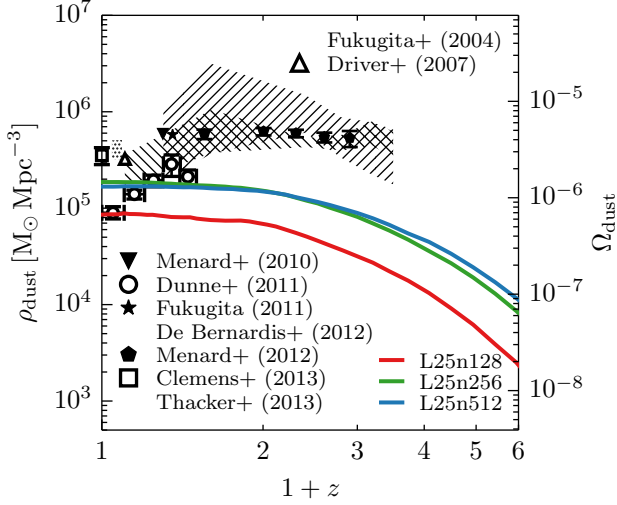


Figure 4. Evolution of the comoving cosmic dust density (ρ_{dust} ; left axis) and associated dust density parameter ($\Omega_{\text{dust}} = \rho_{\text{dust}}/\rho_{\text{c}}$; right axis) as a function of redshift for our three resolution simulations (coloured lines). Recent observations are shown in black (Fukugita & Peebles 2004; Driver et al. 2007; Ménard et al. 2010; Dunne et al. 2011; Fukugita 2011; De Bernardis & Cooray 2012; Ménard & Fukugita 2012; Clemens et al. 2013; Thacker et al. 2013). Filled points include the contribution of dust from haloes, while open points and shaded regions track only galactic dust. The $z = 0$ value of $\Omega_{\text{dust}} \approx 1.3 \times 10^{-6}$ is similar to observational estimates, though the simulated cosmic dust density doesn't display the observed decline from $z = 1$ to $z = 0$.

rected as in Figure 2 to conform to the cosmology that we adopt for our simulations and, where appropriate, the dust mass absorption coefficient used in Dunne et al. (2011). In our simulations, the cosmic dust density is computed by summing the dust masses of all gas cells and dividing by the total comoving volume of $(25 h^{-1} \text{ Mpc})^3$. We also show the cosmic dust density parameter $\Omega_{\text{dust}} \equiv \rho_{\text{dust}}/\rho_{\text{c}}$. In our fiducial simulations, the cosmic dust density increases by over 1 dex from $z = 5$ to $z = 0$, although there is very little evolution for $z < 1.5$ as the cosmic star formation rate density declines. Compared to the DMFs presented in Figure 2, the cosmic dust density results presented Figure 4 show stronger convergence. In particular, the L25n256 and L25n512 runs produce ρ_{dust} values that differ by less than 0.1 dex for $z < 2$. Even the low-resolution L25n128 run displays the same qualitative behaviour with a lower normalisation. This suggests that convergence is less of an issue when looking at volume-integrated dust quantities.

At $z = 0$, the L25n512 run reaches the values $\rho_{\text{dust}} \approx 2 \times 10^5 M_{\odot} \text{ Mpc}^{-3}$ and $\Omega_{\text{dust}} \approx 1.3 \times 10^{-6}$, in rough agreement with various low-redshift observations. In comparison, integrating the best-fitting Schechter function for the L25n512 DMF yields $\Omega_{\text{dust}} \approx 6 \times 10^{-7}$ for the dust content of the ISM at $z = 0$. However, we do not reproduce the observed decline in ρ_{dust} by about a factor of three from $z \approx 0.35$ to $z = 0$ seen in Herschel ATLAS data (Dunne et al. 2011). This decline has had a similar effect on the DMF for this redshift range, causing a drop in the Schechter function parameter M_{dust}^* and shifting the DMF to lower dust masses. The redshift behaviour of the cosmic dust density is not as well-studied as those of the cosmic star formation rate density and stellar mass density (e.g. see Madau & Dickinson 2014, and references therein) and would benefit from additional observations. We note that observations of the stellar mass density ρ_* show an increase of

more than 1.5 dex from $z = 5$ to $z = 0$ and a flattening for $z < 1$, results similar to our simulated ρ_{dust} evolution.

Observational estimates of ρ_{dust} at low redshift have been obtained in a number of ways. One method includes fitting a Schechter function to DMF data and integrating it against dust mass to find $\rho_{\text{dust}} = \Gamma(2 + \alpha) \Phi^* M_{\text{dust}}^*$, where α , Φ^* , and M_{dust}^* are the best-fitting Schechter parameters (Dunne et al. 2011). Others assume a constant ratio between dust mass and B -band luminosity and calculate ρ_{dust} by scaling the observed cosmic luminosity density (Driver et al. 2007). The integrated dust density can also be estimated by transforming the luminosity function obtained from photometric surveys (Clemens et al. 2013) or derived from far-infrared power spectrum measurements (De Bernardis & Cooray 2012; Thacker et al. 2013), or by combining a constant dust-to-metal ratio, mean ISM metallicity, and cool gas density parameter (Fukugita & Peebles 2004). We note, however, that these calculations tend to underestimate or neglect dust in galactic haloes, which is thought to contribute almost as much to Ω_{dust} as ISM dust (Ménard et al. 2010; Fukugita 2011). Dust surface density profiles like in Figure 3, observationally obtained through quasar-galaxy reddening measurements (Ménard et al. 2010; Ménard & Fukugita 2012), can be integrated out to the virial radius to estimate the halo component of dust mass and in turn a value of ρ_{dust} that includes contributions from the ISM and CGM.

The measurement of Ω_{dust} by Ménard et al. (2010) in Figure 4 accounts for dust in galactic haloes and lies above other low-redshift observations. This suggests that calculations of ρ_{dust} and Ω_{dust} using galactic DMFs tracing ISM luminosity or metallicity data may be underestimating the true cosmic dust density, especially in cases where galactic outflows can drive dust away from the ISM. The results in Figures 3 and 4 also show that Σ_{dust} and ρ_{dust} are interconnected: the dust content of the ISM cannot be varied independently of the dust content in galactic haloes, and ρ_{dust} is influenced by dust in both of these regions. To a large degree, ρ_{dust} determines the normalisation of quantities like Σ_{dust} and can be used to put constraints on the typical dust surface density seen for individual galaxies.

3.4 Dust on the Star Formation Main Sequence

Figure 5 shows two-dimensional histograms indicating the average dust mass of galaxies on and around the star formation main sequence at $z = 2.5$ and 0.0 . The average dust mass tends to increase with both stellar mass and SFR as seen in both starburst (Magnelli et al. 2012; Santini et al. 2014) and local galaxies (Draine et al. 2007; Leroy et al. 2007; Kennicutt et al. 2009; Galametz et al. 2011; Skibba et al. 2011; Fisher et al. 2013). For fixed stellar mass or SFR, average dust mass increases from $z = 2.5$ to $z = 0.0$, even as the global SFR density and thus the stellar injection rate of dust drops.

We analyse the dependence of dust mass on stellar mass and SFR using a least-squares fit to the functional form

$$\log \left(\frac{M_{\text{dust}}}{M_{\text{dust},0}} \right) = \alpha \log \left(\frac{M_*}{10^{10} M_{\odot}} \right) + \beta \log \left(\frac{\text{SFR}}{M_{\odot} \text{ yr}^{-1}} \right), \quad (6)$$

where $M_{\text{dust},0}$, α , and β are free parameters. We apply this fit to all galaxies within 1σ of the star formation main sequence, using the best-fitting relations from Figure 7 of Torrey et al. (2014). (The $z = 2.0$ main sequence relation in that work is used for our $z = 2.5$ panel.) We also impose the cut $M_* > 10^7 M_{\odot}$ to avoid galaxies that lie at the poorly-resolved end of the galaxy stellar mass function. At $z = 2.5$, the best-fitting parameters are

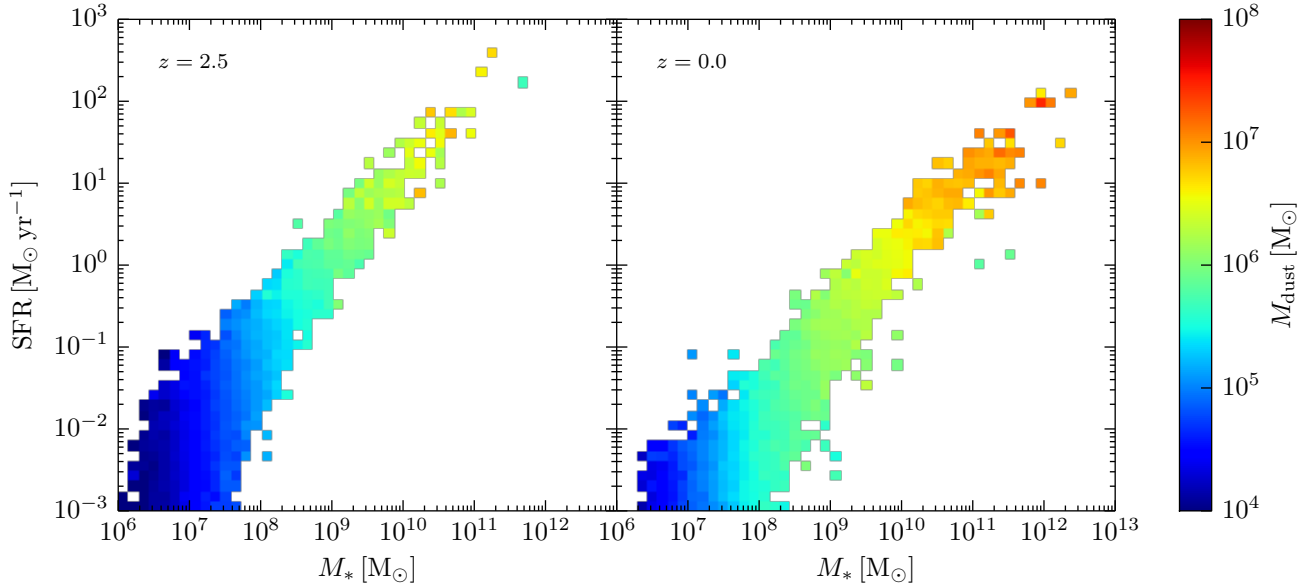


Figure 5. Star formation main sequence at $z = 2.5$ (left) and $z = 0.0$ (right) for our L25n512 run, where the colour of each bin denotes the average dust mass of galaxies whose stellar mass and SFR fall in those intervals. At both redshifts, dust mass tends to increase with stellar mass and SFR, though the correlation is stronger for stellar mass.

$M_{\text{dust},0} = 2.3 \times 10^6 M_{\odot}$, $\alpha = 0.55$, and $\beta = 0.11$, while at $z = 0.0$ they are $M_{\text{dust},0} = 3.7 \times 10^6 M_{\odot}$, $\alpha = 0.43$, $\beta = 0.09$. Dust mass is largely predicted by stellar mass, although there is also a weak scaling with SFR.

Figure 5 suggests that it is reasonable to associate the dustiest galaxies with those that are the most star-forming. Such a procedure is used in some hydrodynamical simulations where dust is not directly treated in order to study the highly-luminous, dust-rich submillimetre population. For example, Davé et al. (2010) assumes a $z \sim 2$ submillimetre galaxy number density of $1.5 \times 10^{-5} \text{ Mpc}^{-3}$ based on observations (Chapman et al. 2005; Tacconi et al. 2008) and finds that an SFR cut of around $180 M_{\odot} \text{ yr}^{-1}$ produces a galaxy population with a similar number density. This highly star-forming population is taken to be the submillimetre set.

However, we caution that the relation between dust mass, stellar mass, and SFR is complex, especially for submillimetre galaxies. Our boxes of side length $25 h^{-1} \text{ Mpc}$ have difficulty capturing the nuclear starbursts and main sequence outliers (Sparre et al. 2015; Sparre & Springel 2016) that tend to simultaneously increase the SFR and decrease the dust mass (Hayward et al. 2011). Radiative transfer predicts that submillimetre flux scales more strongly with dust mass than SFR, and Figure 5 indicates dust mass is most strongly predicted by stellar mass. Comparing a low-stellar mass starburst with a higher-mass, lower-SFR main sequence galaxy, the latter may have higher submillimetre flux because its increased dust mass more than compensates for its smaller SFR.

3.5 Scaling and Evolution of Dust-to-Stellar Mass Ratio

A galaxy’s dust-to-stellar mass ratio can increase not only through dust injected into the ISM during stellar evolution, but also through subsequent dust growth in collisions with interstellar gas. Chemical evolution models (e.g. based on the work in Edmunds 2001) suggest that stellar injection of dust by itself – with no ISM dust growth – only produces dust-to-stellar mass ratios around 10^{-3} or

less. Even in the extreme scenario where SNe produce more dust than observed and condense nearly all ejected metals, this only results in dust-to-stellar mass ratios near 10^{-2} (Dunne et al. 2011; Bourne et al. 2012). We predict some galaxies with dust-to-stellar mass ratios around 10^{-2} , and such dust-to-stellar mass ratios have been observed (Bourne et al. 2012; Cortese et al. 2012). Unless dust condensation efficiencies are much higher than expected, this suggests that ISM dust growth is an important contributor to high dust-to-stellar mass ratios. We note that previous works have analyzed the relative strengths of interstellar dust growth and stellar injection of grains for increasing a galaxy’s dust-to-gas ratio (Mattsson, Andersen & Munkhammar 2012; Mattsson & Andersen 2012). By studying a population of galaxies, we can investigate both galaxies whose dust-to-stellar mass ratios are driven by stellar injection of grains and by ISM dust growth.

In Figure 6, we show the distribution of our simulated galaxies as a function of dust-to-stellar mass ratio and stellar mass as well as dust-to-stellar mass ratio and specific star-formation rate (sSFR) at $z = 2.5, 1.0$, and 0.0 . We compare with multiple sources of observational data, detailed in Table 3 and meant to capture a variety of morphological types, colours, and metallicities, and note that sSFR anti-correlates with stellar mass (Brinchmann et al. 2004; Salim et al. 2007; Karim et al. 2011; Whitaker et al. 2012; Abramson et al. 2014; Knebe et al. 2015). Several of the data sets in Table 3 were already binned across stellar mass or sSFR or provided a mean result which we show, together with quoted uncertainties, without modification in Figure 6. For those unbinned data sets comprised of numerous individual galaxy observations, we manually bin the data to improve plot readability and compute sample standard deviations in log-space to obtain symmetric error bars for Figure 6.

The median sSFR drops by over 1 dex from $z = 2.5$ to 0.0 as the median dust-to-stellar mass ratio is largely unchanged. The scatter in dust-to-stellar mass ratio at fixed sSFR slightly increases towards low redshift. However, the slope of the dust-to-stellar mass ratio versus stellar mass relation does not change appreciably from

Table 3. Observational references with dust-to-stellar mass ratio data shown in Figure 6. We provide an approximate redshift range corresponding to our cosmology for each sample and list the redshift at which data is plotted in Figure 6. In the last column, we briefly characterize each sample of galaxies and clarify which data we use. Several references provided already-binned data with uncertainties capturing scatter about the mean. For those references that provided quantities on a galaxy-by-galaxy basis, we binned data ourselves, calculating uncertainties in log-space to provide symmetric error bars for Figure 6.

Reference	Abbreviation	Redshift Range	Redshift Panel	Notes
da Cunha et al. (2010)	D10	$z < 0.22$	$z = 0.0$	we bin the sample of galaxies observed in all four IRAS bands
Dunne et al. (2011)	D11	$z < 0.5$	$z = 0.0$	we use the mean result for these late-type galaxies
Skibba et al. (2011)	S11	$z < 0.01$	$z = 0.0$	we use the mean result for galaxies of all morphological types
Bourne et al. (2012)	B12-B	$z < 0.35$	$z = 0.0$	already-binned sample of galaxies with blue $g - r$ colour
	B12-G	$z < 0.35$	$z = 0.0$	already-binned sample of galaxies with green $g - r$ colour
	B12-R	$z < 0.35$	$z = 0.0$	already-binned sample of galaxies with red $g - r$ colour
Cortese et al. (2012)	C12-N	$z < 0.01$	$z = 0.0$	already-binned sample of H I-normal galaxies
	C12-D	$z < 0.01$	$z = 0.0$	already-binned sample of H I-deficient galaxies
Davies et al. (2012)	D12	$z < 0.01$	$z = 0.0$	we bin this sample of bright galaxies
Rowlands et al. (2012)	R12	$z < 0.5$	$z = 0.0$	we bin the sample of early-type galaxies
Smith et al. (2012)	S12	$z < 0.01$	$z = 0.0$	we bin the sample of early-type galaxies, excluding non-detections
Santini et al. (2014)	S14	$0.6 < z < 1.5$	$z = 1.0$	we bin this sample of galaxies
	S14	$1.5 < z < 2.5$	$z = 2.5$	we bin this sample of high-redshift galaxies
Rémy-Ruyer et al. (2015)	R15	$z < 0.05$	$z = 0.0$	we bin the sample covering a roughly 2 dex metallicity range

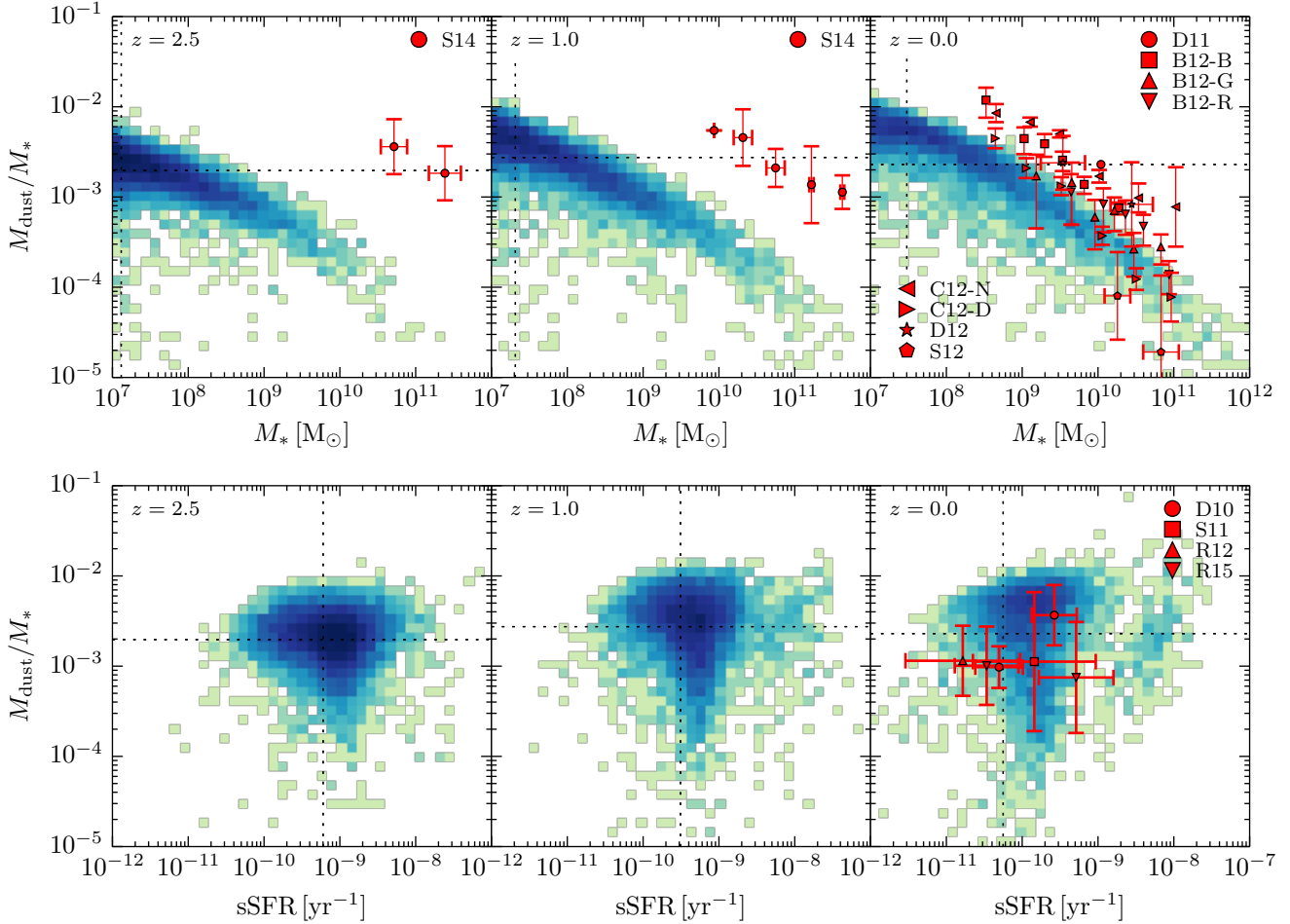


Figure 6. Dust-to-stellar mass ratio (M_{dust}/M_*) as a function of stellar mass (top row) and specific star-formation rate (sSFR; bottom row) at $z = 2.5$, 1.0, and 0.0 (left, middle, and right panels). For each redshift, the logarithmic distribution of simulated galaxies in the L25n512 run is given by a two-dimensional histogram, with bluer colours indicating greater density. Dotted black lines mark the median value in the distribution for each axis. References for the binned observational data (red points) are given in Table 3. Dust-to-stellar mass ratio anti-correlates with stellar mass at both high and low redshift.

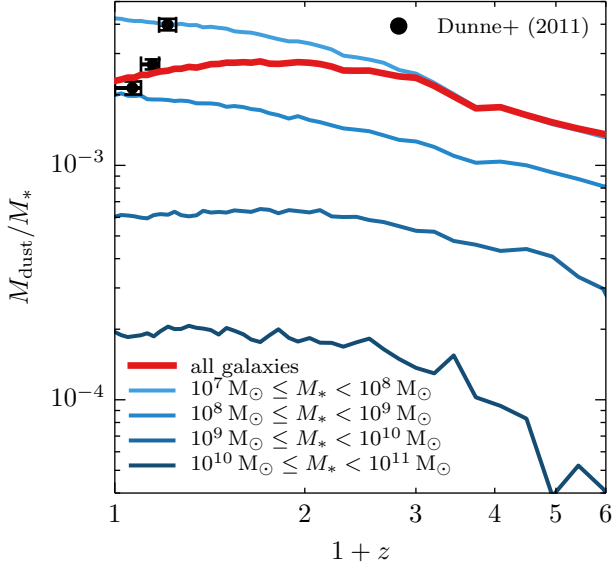


Figure 7. Evolution of the galactic dust-to-stellar mass ratio (M_{dust}/M_*) as a function of redshift for the L25n512 run. We compute the median dust-to-stellar mass ratio for all galaxies (red line) and for different stellar mass bins (blue lines, with deeper shades indicating greater stellar mass), excluding galaxies with no stellar component. Observational data using galaxies with spectroscopic redshifts from the Herschel ATLAS (Dunne et al. 2011) are shown in black, though we note these observations were not binned by mass. The median dust-to-stellar mass ratio increases by about a factor of 1.7 from $z = 5$ to $z = 0$, with the most massive galaxies displaying less evolution in dust-to-stellar mass ratio.

$z = 2.5$ to $z = 0.0$. At high redshift, the observed dust-to-stellar mass ratios for $M_* \gtrsim 10^{10} M_\odot$ from Santini et al. (2014) are larger than what we predict. However, we note that most of the high-redshift galaxies in Santini et al. (2014) have $\text{SFR} \gtrsim 100 M_\odot \text{ yr}^{-1}$, making them more star-forming than nearly all galaxies in our simulation.

To better understand the connection between dust-to-stellar mass ratio and stellar mass, in Figure 7 we plot the median dust-to-stellar mass ratio as a function of redshift for 1 dex stellar mass bins ranging from $10^7 M_\odot$ to $10^{11} M_\odot$, along with the median ratio across all simulated galaxies. The results from Figure 6 – that the dust-to-stellar mass ratio decreases with increasing stellar mass, while the overall median dust-to-stellar mass ratio does not substantially increase with time – are confirmed in Figure 7. The nature of the galaxy stellar mass function implies that at nearly every redshift the median dust-to-stellar mass ratio lies nearer to the ratio for $10^7 M_\odot < M_* < 10^9 M_\odot$ galaxies than for more massive galaxies.

The overall median dust-to-stellar mass ratio increases by just under a factor of two from $z = 5$ to 0, and it is largely flat for $z < 1$. Low stellar mass galaxies display similar behaviour, while the dust-to-stellar mass ratio for large galaxies with $M_* > 10^{10} M_\odot$ is roughly 1 dex below the value for galaxies with $10^7 M_\odot < M_* < 10^9 M_\odot$. However, we do not capture the decrease in dust-to-stellar mass ratio by a factor of two observed in Herschel ATLAS data for $z < 0.5$ (Dunne et al. 2011), a result similarly shown in Figure 4.

While the dust-to-stellar mass scaling at $z = 0$ is in decent agreement with observations, the relation between dust-to-gas ratio and gas-phase metallicity displays more tension and a greater sensitivity to the parameters of our model. In Figure 8, we plot

the dust-metallicity relation at $z = 0$ for the L25n256 and M16 model simulations and offer a comparison to observations (Leroy et al. 2011; Rémy-Ruyer et al. 2014) and modelling (Asano et al. 2013a; Zhukovska 2014; Popping, Somerville & Galametz 2016). It is clear that the L25n256 run fails to match slope of the expected dust-metallicity relation: despite offering a reasonable fit to the $z = 0$ DMF in Figure 2, the dust-metallicity relation is far too flat. The L25n256 run is similar to the semi-analytic model of Popping, Somerville & Galametz (2016) for $12 + \log(\text{O}/\text{H}) < 8$, but deviates strongly at high metallicity. The dust growth timescale in large galaxies in the L25n256 run seems to be too long, preventing them from rapidly growing their dust mass. On the other hand, the M16 model – which employs a stronger ISM dust growth mechanism and lacks thermal sputtering – displays a dust-metallicity relation whose slope better matches observations but whose normalisation is too high. However, the M16 model significantly overproduces dust-rich galaxies in its $z = 0$ DMF. Figure 8 offers another look at the DMF tension in Figure 2 and highlights the difficulty in producing enough dust to match the dust-metallicity relation while avoiding a DMF with too many dust-rich galaxies.

3.6 Stellar Population Synthesis Postprocessing

We can combine the direct dust mass tracking in our work with stellar population synthesis postprocessing to make predictions about the observational properties of simulated galaxies. One such property is the dust-to-stellar flux ratio (f_{dust}/f_*), which measures the flux reradiated by dust grains as a fraction of unextincted stellar flux and has been observed to correlate with dust mass and infrared luminosity (Skibba et al. 2011). Below, we use the FSPS (Conroy, Gunn & White 2009; Conroy & Gunn 2010) stellar population synthesis code to estimate each galaxy’s bolometric luminosity and in turn its dust-to-stellar flux ratio.

The dependence of optical depth on host galaxy properties was previously modelled in Jonsson et al. (2006). Following Table 2 in Jonsson et al. (2006), we estimate the bolometric attenuation to be

$$\tau = 0.93 \left(\frac{Z}{0.02} \right)^{1.10} \left(\frac{\text{SFR}}{M_\odot \text{ yr}^{-1}} \right)^{0.61} \left(\frac{M_b}{10^{11} M_\odot} \right)^{-0.68}, \quad (7)$$

where M_b is the galaxy’s total baryon mass. We calculate τ directly on a galaxy-by-galaxy basis using our SUBFIND output. We compute an unattenuated synthetic spectral energy distribution (SED) for every star particle as a function of its initial mass, age, and metallicity, assuming a Chabrier (2003) IMF, and define a galaxy’s SED to be the sum of those from constituent star particles. For a galaxy with bolometric luminosity L and optical depth τ computed in Equation (7), we calculate the dust luminosity L_{dust} using Equation 6 in Jonsson et al. (2006),

$$L_{\text{dust}}/L = 1 - (1/\tau)(1 - e^{-\tau}). \quad (8)$$

The stellar luminosity is then $L_* = L - L_{\text{dust}}$. In essence, stellar flux is computed by integrating the attenuated stellar SED, and dust flux is obtained by integrating over the difference between the unattenuated and attenuated stellar SEDs. This calculation of the dust-to-stellar flux ratio is simpler than estimating and removing stellar emission in the mid-infrared from a dust-extincted SED (Draine et al. 2007; Muñoz-Mateos et al. 2009; Skibba et al. 2011), although only possible when postprocessing simulated galaxies.

Figure 9 shows the distribution of galaxies in the L25n512 run as a function of dust-to-stellar flux and mass ratios at $z = 0$, with observational data from the Herschel KINGFISH Survey overlaid (Skibba et al. 2011). While the range of dust-to-stellar mass ratios

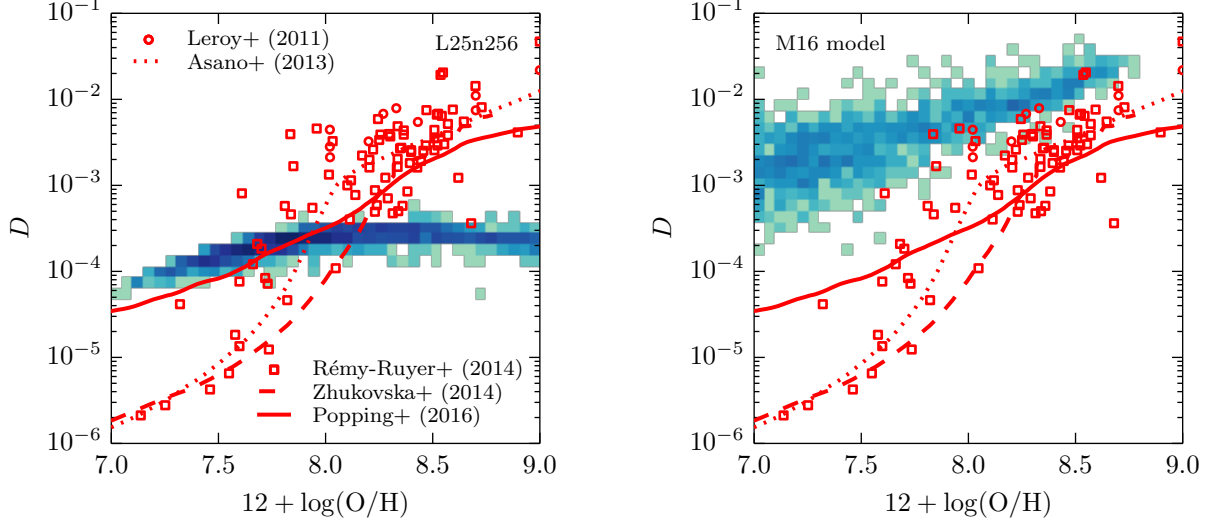


Figure 8. Simulated dust-metallicity relations at $z = 0$ for the fiducial L25n256 run (left) and M16 model (right). The two-dimensional histograms use a logarithmic colourscale to indicate number density, with bluer colours denoting a greater number of galaxies at a given dust-to-gas ratio and metallicity. Red points and lines denote observational data (Leroy et al. 2011; Rémy-Ruyer et al. 2014) and results from analytic and semi-analytic modelling (Asano et al. 2013a; Zhukovska 2014; Popping, Somerville & Galametz 2016). To improve readability, we omit error bars. From Asano et al. (2013a) we use the $\tau_{\text{SF}} = 5$ Gyr model and from Zhukovska (2014) we use the “6x 500 Myr bursts $\tau_{\text{SF}} = 2$ Gyr” model, which were compiled by Rémy-Ruyer et al. (2014).

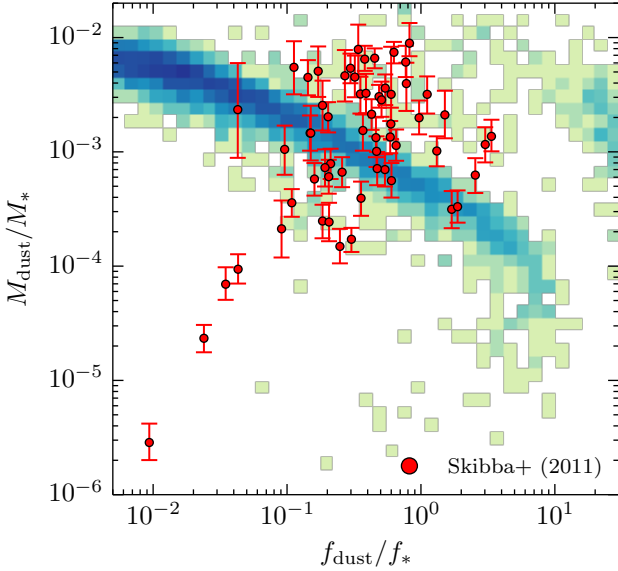


Figure 9. Dust-to-stellar mass ratio (M_{dust}/M_*) as a function of dust-to-stellar flux ratio (f_{dust}/f_*) at $z = 0$. The two-dimensional histogram shows the number distribution of galaxies from the L25n512 run on a logarithmic scale, with bluer colours denoting greater counts. We compare with observational data (red circles) from the Herschel KINGFISH Survey (Skibba et al. 2011).

does tend to match these observations, the simulated dust-to-stellar flux ratios are biased to smaller values than in the Herschel KINGFISH set. The two-dimensional distribution of simulated galaxies peaks near $M_{\text{dust}}/M_* \approx 5 \times 10^{-3}$ and $f_{\text{dust}}/f_* \approx 2 \times 10^{-2}$, though there is significant scatter in the dust-to-stellar flux ratios, with a number of galaxies recording $f_{\text{dust}}/f_* > 1$. The largest tension with observations comes at low dust-to-stellar flux ratio, where

we predict numerous galaxies with large dust-to-stellar mass ratio. From Figure 6, we know that galaxies with high dust-to-stellar mass ratios tend to have low stellar masses and thus low metallicities and SFRs. This may drive down the optical depths calculated in Equation (7) and thus the dust-to-stellar flux ratios. Several of the galaxies in Skibba et al. (2011) with low dust-to-stellar flux ratios are early-types, which are known to have smaller dust-to-stellar mass ratios on average than spirals (Rowlands et al. 2012; Smith et al. 2012). In any case, the scatter in our simulated results does confirm the observation that the dust-to-stellar flux ratio covers roughly three orders of magnitude and does not effectively constrain the mass ratio (Skibba et al. 2011).

Previous works have demonstrated how hydrodynamical simulations without direct dust tracking can be coupled with radiative transfer to study galactic flux densities at submillimetre wavelengths (Chakrabarti et al. 2008; Narayanan et al. 2009, 2010; Hayward et al. 2011, 2012, 2013). Performing dust radiative transfer on simulations of isolated and merging disc galaxies, Hayward et al. (2011) developed fitting functions to estimate submillimetre flux densities in the SCUBA 850 μm and AzTEC 1.1 mm bands as a function of SFR and dust mass as well as dust luminosity and dust mass. While these relations were derived from simulations investigating number counts of bright submillimetre galaxies, here we apply them to our full sample of galaxies to demonstrate how cosmological simulations can benefit from results obtained through radiative transfer calculations.

To construct submillimetre number densities, we define the Hubble parameter $H(z) = H_0 \sqrt{\Omega_m(1+z)^3 + \Omega_\Lambda}$ and comoving distance

$$l_c(z) = \int_0^z \frac{cdz'}{H(z')}. \quad (9)$$

If $\Phi(S, z)$ denotes the comoving number density of galaxies with submillimetre flux S at redshift z per unit logarithmic flux, then

$$\phi(S) = \left(\frac{\pi}{360^2} \text{deg}^{-2}\right) \int_0^\infty 4\pi l_c(z)^2 \Phi(S, z) dl_c(z) \quad (10)$$

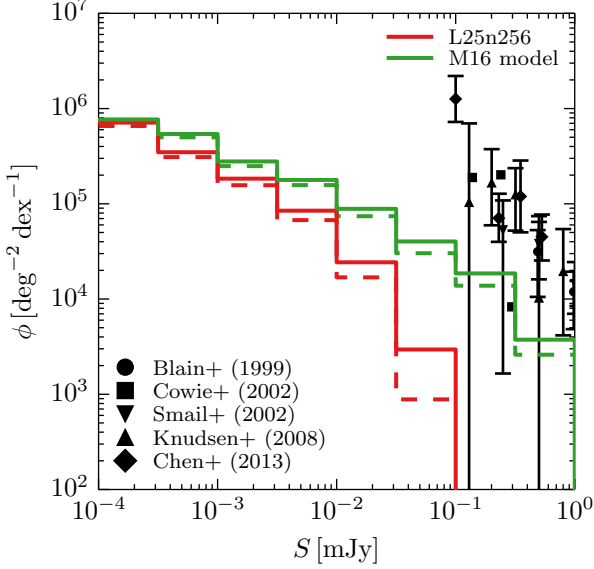


Figure 10. Simulated number density functions in the SCUBA $850\ \mu\text{m}$ band for the fiducial L25n256 run (red) and the M16 model (green). Fluxes are computed using the luminosity- and dust mass-dependent fitting functions provided in Hayward et al. (2011). Black points mark observations for $850\ \mu\text{m}$ (Blain et al. 1999a; Smail et al. 2002; Cowie, Barger & Kneib 2002; Knudsen, van der Werf & Kneib 2008; Chen et al. 2013) as compiled by Casey, Narayanan & Cooray (2014). Because the fits in Hayward et al. (2011) were not designed for $z \lesssim 1$, we show two versions of the number density functions: one integrated all the way down to $z = 0$ (solid lines) and the other only down to $z = 1$ (dashed lines). The versions show similar behaviour. While the M16 model offers a better fit to the observed submillimetre number densities and the high-redshift DMF in Figure 2, it significantly overproduces dust in the $z = 0$ DMF.

is the number of galaxies with flux S per square degree per unit logarithmic flux. Simplifying, we calculate submillimetre number counts using

$$\phi(S) = \left(\frac{\pi}{360^2} \text{deg}^{-2} \right) \int_0^\infty 4\pi l_c(z)^2 \Phi(S, z) \frac{c}{H(z)} dz. \quad (11)$$

In practice, we numerically integrate Equation (11) using $\Phi(S, z)$ values constructed from simulation output at discrete redshifts.

Number density functions for simulated galaxies at $850\ \mu\text{m}$ are shown in Figure 10 for our fiducial L25n256 run and the M16 model. We compare with various observational data (Blain et al. 1999a; Smail et al. 2002; Cowie, Barger & Kneib 2002; Knudsen, van der Werf & Kneib 2008; Chen et al. 2013). Fluxes in this band are computed using dust luminosities and dust masses following Equation 2 and Appendix A in Hayward et al. (2011). Dust luminosities are calculated as in the construction of Figure 9. Because the fits provided in Hayward et al. (2011) are not designed to apply to $z \lesssim 1$, we compute number density functions in two ways: one using $z = 0$ as the lower limit of the integration in Equation (11) and the other using $z = 1$. This variation changes results only slightly. Results for this submillimetre band show that the number density of galaxies declines over the flux interval $10^{-4} \text{ mJy} < S < 10^{-1} \text{ mJy}$ accessible in both simulations. The M16 model offers a much better fit to the high-flux observations than the L25n256 run, in large part because the high-redshift DMF for M16 model in Figure 2 contains many more dust-rich galaxies. However, despite the more realistic submillimetre num-

ber counts, the M16 model has tension of its own: its $z = 0$ DMF contains far too many galaxies with $M_{\text{dust}} > 10^8 M_\odot$. This tension highlights the need to form enough dust at high redshift to generate realistic submillimetre number counts while preventing an excess of dust at low redshift. Furthermore, as noted in our discussion of the star formation main sequence in Figure 5, the box length of $L = 25 h^{-1} \text{ Mpc}$ used in this work makes it difficult to truly probe the submillimetre regime and uncover possible exponential cutoffs in the submillimetre number density functions. This may be worth pursuing in cosmological simulations of larger volumes or in semi-analytic models with dust tracking.

4 DISCUSSION

We have presented full volume cosmological simulations with a model for dust production and destruction to study the coevolution of dust and galaxies. Our model offers rough agreement with low-redshift observations of the DMF, cosmic dust density, and relation between dust-to-stellar mass ratio and stellar mass, but it also highlights limitations that appear more fundamental. Despite offering a reasonable match to the $z = 0$ DMF, the fiducial model fails to capture the abundance of dusty galaxies at high redshift and instead produces galaxies whose dust masses grow roughly in a monotonic fashion. It has been suggested that perhaps the dust-rich galaxies at high redshift have extra-high star-formation efficiencies, are more efficient at forming dust from stars, or feature more top-heavy IMFs than low-redshift galaxies (Dunne et al. 2011). In this scenario, the most dusty galaxies at $z = 2.5$ could evolve to the present with much lower dust masses after consuming their gas and dust in star formation. The ability of the fiducial model to roughly match the $z = 0$ DMF but not capture the decline in dusty galaxies from high to low redshift suggests that dust evolution processes may be more dependent on host galaxy properties like SFR or gas fraction than assumed in this work. For example, dust yields in stellar ejecta may be a function of local ISM density or temperature, which evolve with redshift. To account for the observed shift towards lower masses in the DMF from $z = 2.5$ to $z = 0$, we need efficient sputtering of grains in dust-rich galaxies. This would better enable different galaxies to have diverse dust mass histories and perhaps lead to DMF behaviour that more closely follows the cosmic SFR evolution (e.g. see Madau & Dickinson 2014, and references therein).

Our analysis of the DMF, dust surface density profiles, and cosmic dust density evolution also highlights the observational uncertainties that make it challenging to obtain reliable dust mass estimates. For example, the dust surface density comparison in Figure 3 shows that our simulated dust radial profiles are closest to observations from SDSS out to $r \approx 30 \text{ kpc}$ but lie below observations by up to 1 dex at larger radii. The cosmic dust density in our simulations could easily absorb a factor of two or three increase and still be consistent with observations in Figure 4, and such a normalisation change would help boost the dust surface density profiles on a global scale. This change is plausible since dust condensation efficiencies in stellar ejecta and ISM growth time-scales are not well-constrained. Independent of such a normalisation shift, it is also possible that thermal sputtering is slightly too strong or galactic outflows too weak, limiting the amount of dust in galactic haloes.

The sample of SDSS galaxies used to construct surface density profiles in Ménard et al. (2010) has a redshift distribution that peaks at $z \approx 0.3$ but with a full-width at half-maximum of 0.4. While we do not predict much evolution in the cosmic dust den-

sity for $z \lesssim 1$, the fact that Figure 3 is constructed at a fixed redshift of $z \approx 0.3$ may introduce some deviation in surface density profiles from the observed result. The observed reddening signal was also tested for possible systematic effects (e.g. by subsampling quasars according to magnitude bins or using sky regions with different Galactic reddening) and found to be robust. The calculations in Ménard et al. (2010) assume SMC-type dust, motivated in part by the observation that few high-redshift galaxies share the $0.2 \mu\text{m}$ extinction curve bump characteristic of the Milky Way, but adopting Milky Way-type dust would change dust masses about a factor of two. Given the difficulties in estimating dust masses from reddening signals, including weak constraints on dust mass absorption coefficients, the discrepancies between simulated and observed dust surface density profiles could be influenced by inaccuracies in modelled physics like thermal sputtering or galactic outflows or by uncertain observational assumptions. The Ménard et al. (2010) relation can possibly be used as a constraint on outflow physics, as the dust surface density profiles at large radii are likely sensitive to the outflow model and the coupling of dust and gas in winds. In our simulations, we assume winds have the same depletion as the ISM from which they are launched (e.g. if a wind particle is created in a cell where 10% of metals are locked in dust, then 10% of the metal content of the wind particle is assumed to be dust), but alternative models that couple dust more strongly to winds may help drive dust to Mpc distances. Simulations by Zu et al. (2011) suggest that reproducing the Ménard et al. (2010) relation without galactic winds is difficult, and the strength of outflows could be used to constrain enrichment in the intergalactic medium.

While dust masses can be hard to estimate, the findings in Section 3.5 demonstrate the connection between a galaxy’s stellar mass and its dust content. For example, Figure 7 provides a method to calculate a galactic dust mass when only the stellar mass and redshift are known, using the dust-to-stellar mass ratio in the appropriate stellar mass bin. Both Figures 6 and 7 highlight the dependence of dust-to-stellar mass ratio on stellar mass and why assuming a uniform dust-to-stellar mass ratio is not ideal. Previous observational studies have shown that gas fraction and molecular gas fraction decrease with stellar mass (Leroy et al. 2008; Daddi et al. 2010; Geach et al. 2011; Saintonge et al. 2011; Popping et al. 2012; Bauermeister et al. 2013; Tacconi et al. 2013; Boselli, Cortese & Boquien 2014; Bothwell et al. 2014; Morokuma-Matsui & Baba 2015), and this result has been reproduced in galaxy formation simulations and semi-analytic models (Hopkins et al. 2009; Obreschkow et al. 2009; Davé et al. 2010; Lagos et al. 2011a,b; Duffy et al. 2012; Fu et al. 2012; Genel et al. 2014; Popping, Somerville & Trager 2014; Lagos et al. 2015; Narayanan et al. 2015). Additionally, simple dust and chemical evolution models suggest that the dust-to-stellar mass ratio increases with gas fraction (Dunne et al. 2011), a result that has been seen in Herschel Reference Survey data (Cortese et al. 2012).

Together, these findings indicate the dust-to-stellar mass ratio should be largest in low stellar mass systems, a result that agrees with the negative slope of dust-to-stellar mass ratio versus stellar mass shown in Figures 6 and 7. These less massive galaxies have high sSFRs that allow the injection of dust from stellar sources more quickly than in larger systems, and since their sSFRs peak later than those of more massive galaxies (Cowie et al. 1996), smaller galaxies can see more growth in the dust-to-stellar mass ratio. Knowing a galaxy’s stellar mass, and its star-formation history, allows us to better estimate its dust content.

5 CONCLUSIONS

In this work, we extended the dust model in the moving-mesh code AREPO to account for thermal sputtering of grains and performed cosmological hydrodynamical simulations to analyse the evolution of dust in a diverse sample of galaxies. We studied the evolution of the DMF, the radial distribution of dust in galactic haloes and on Mpc scales, and the contribution of dust to the cosmic mass budget. Also, we explored how a galaxy’s SFR and stellar mass impacts its dust content. Our main conclusions are as follows:

(i) Our model broadly reproduces the observed $z = 0$ DMF over the range of masses accessible in a $(25 h^{-1} \text{Mpc})^3$ volume. The DMF is presented for simulations at three resolutions, with the highest-resolution simulation softening $z = 0$ gravitational forces on scales of $625 h^{-1} \text{pc}$.

(ii) The mean dust surface density profile for simulated galaxies with $17 < i < 21$ at $z = 0.3$ declines with radial distance, similar to the $\Sigma_{\text{dust}} \propto r^{-0.8}$ scaling seen in SDSS data out to projected distances of 10 Mpc, although the normalisation of the simulated dust surface density lies up to 1 dex below observations for $r \gtrsim 100 \text{kpc}$.

(iii) The cosmic dust density parameter at $z = 0$ is estimated to be $\Omega_{\text{dust}} = 1.3 \times 10^{-6}$, close to values obtained from low-redshift observations. We see little evolution in Ω_{dust} for $z \lesssim 1.5$, in tension with power spectrum-derived measurements that show a decline of roughly 0.5 dex. This conflict is consistent with our model’s underproduction of dusty galaxies for the high-redshift DMF.

(iv) At both high and low redshift, dust mass increases with stellar mass along the star formation main sequence. This suggests that semi-analytic or galaxy formation models without dust tracking can estimate dust content using the star formation main sequence. Semi-analytic models may also benefit from fitting functions for submillimetre number densities.

(v) The dust-to-stellar mass ratio is predicted to anti-correlate with stellar mass at high and low redshift, and this relation parallels observations at $z = 0$. Less massive systems witness growth in dust-to-stellar mass ratio over $0 < z < 5$. Our simulated galaxies also agree well with the observed distribution of dust-to-stellar mass ratio versus sSFR at $z = 0$.

(vi) By combining direct dust mass tracking with stellar population synthesis postprocessing, we predict dust-to-stellar mass and flux ratios for our simulated galaxies at $z = 0$ and compare to observations. Coupling with empirical relations from radiative transfer simulations, we estimate the high-redshift submillimetre number density functions for our sample of galaxies at $850 \mu\text{m}$.

(vii) While our model reproduces the observed $z = 0$ DMF fairly well, it is unable to capture the abundance of dust-rich galaxies at high redshift. Instead, the simulated DMF evolves in a fairly monotonic fashion. Adopting a top-heavy IMF does increase the abundance of high-redshift dusty galaxies but not to the extent seen in observations.

(viii) To better match the observed DMF evolution, we may need physical prescriptions that are more closely connected to the behaviour of the cosmic SFR density and produce more dusty galaxies near the peak of star formation. For example, adopting non-constant dust condensation efficiencies that vary with ISM density and temperature may allow the largest galaxies to more efficiently produce dust at high redshift but limit dust formation at lower redshifts where star formation is less efficient and the DMF shifts towards lower masses.

The dust model presented in this work yields low-redshift re-

sults in rough agreement with a number of observables across a diverse sample of galaxies, but it also highlights areas of tension. In particular, this model fails to predict the abundance of dust-rich galaxies at high redshift and the slight decline in Ω_{dust} as galaxies evolve towards low redshift. Furthermore, to truly probe the high-redshift submillimetre regime and the massive end of the DMF will require larger cosmological volumes. Nonetheless, this work demonstrates how simulations of large galaxy populations can be used to study the evolution of dust across diverse environments and the distribution of dust on cosmological scales.

ACKNOWLEDGEMENTS

We thank Volker Springel for providing us with access to AREPO. We also thank the referee for their constructive feedback.

The simulations were performed on the joint MIT-Harvard computing cluster supported by MKI and FAS. RM acknowledges support from the DOE CSGF under grant number DE-FG02-97ER25308. MV acknowledges support through an MIT RSC award. CCH is grateful to the Gordon and Betty Moore Foundation for financial support.

REFERENCES

- Abramson L. E., Kelson D. D., Dressler A., Poggianti B., Gladsters M. D., Oemler, Jr. A., Vulcani B., 2014, *ApJL*, 785, L36
- Adelberger K. L., Steidel C. C., 2000, *ApJ*, 544, 218
- Asano R. S., Takeuchi T. T., Hirashita H., Inoue A. K., 2013a, *Earth, Planets, and Space*, 65, 213
- Asano R. S., Takeuchi T. T., Hirashita H., Nozawa T., 2013b, *MNRAS*, 432, 637
- Barger A. J., Cowie L. L., Sanders D. B., Fulton E., Taniguchi Y., Sato Y., Kawara K., Okuda H., 1998, *Nature*, 394, 248
- Barlow M. J., 1978, *MNRAS*, 183, 367
- Bauermeister A., Blitz L., Bolatto A., Bureau M., Teuben P., Wong T., Wright M., 2013, *ApJ*, 763, 64
- Baugh C. M., Lacey C. G., Frenk C. S., Granato G. L., Silva L., Bressan A., Benson A. J., Cole S., 2005, *MNRAS*, 356, 1191
- Bianchi S., Ferrara A., 2005, *MNRAS*, 358, 379
- Bianchi S., Schneider R., 2007, *MNRAS*, 378, 973
- Blain A. W., Jameson A., Smail I., Longair M. S., Kneib J.-P., Ivison R. J., 1999a, *MNRAS*, 309, 715
- Blain A. W., Kneib J.-P., Ivison R. J., Smail I., 1999b, *ApJL*, 512, L87
- Boselli A., Cortese L., Boquien M., 2014, *A&A*, 564, A65
- Bothwell M. S. et al., 2014, *MNRAS*, 445, 2599
- Bourne N. et al., 2012, *MNRAS*, 421, 3027
- Brinchmann J., Charlot S., White S. D. M., Tremonti C., Kauffmann G., Heckman T., Brinkmann J., 2004, *MNRAS*, 351, 1151
- Bruzual G., Charlot S., 2003, *MNRAS*, 344, 1000
- Burke J. R., Silk J., 1974, *ApJ*, 190, 1
- Casey C. M., Narayanan D., Cooray A., 2014, *Phys. Rep.*, 541, 45
- Chabrier G., 2003, *PASP*, 115, 763
- Chakrabarti S., Fenner Y., Cox T. J., Hernquist L., Whitney B. A., 2008, *ApJ*, 688, 972
- Chakrabarti S., Whitney B. A., 2009, *ApJ*, 690, 1432
- Chapman S. C., Blain A. W., Smail I., Ivison R. J., 2005, *ApJ*, 622, 772
- Chary R., Elbaz D., 2001, *ApJ*, 556, 562
- Chen C.-C., Cowie L. L., Barger A. J., Casey C. M., Lee N., Sanders D. B., Wang W.-H., Williams J. P., 2013, *ApJ*, 762, 81
- Clark C. J. R. et al., 2015, *MNRAS*, 452, 397
- Clemens M. S. et al., 2013, *MNRAS*, 433, 695
- Conroy C., Gunn J. E., 2010, *ApJ*, 712, 833
- Conroy C., Gunn J. E., White M., 2009, *ApJ*, 699, 486
- Cortese L. et al., 2012, *A&A*, 540, A52
- Cowie L. L., Barger A. J., Kneib J.-P., 2002, *AJ*, 123, 2197
- Cowie L. L., Songaila A., Hu E. M., Cohen J. G., 1996, *AJ*, 112, 839
- da Cunha E., Eminian C., Charlot S., Blaizot J., 2010, *MNRAS*, 403, 1894
- Daddi E. et al., 2010, *ApJ*, 713, 686
- Davé R., Finlator K., Oppenheimer B. D., Fardal M., Katz N., Kereš D., Weinberg D. H., 2010, *MNRAS*, 404, 1355
- Davies J. I. et al., 2012, *MNRAS*, 419, 3505
- De Bernardis F., Cooray A., 2012, *ApJ*, 760, 14
- Dey A. et al., 2008, *ApJ*, 677, 943
- Dolag K., Borgani S., Murante G., Springel V., 2009, *MNRAS*, 399, 497
- Draine B. T. et al., 2007, *ApJ*, 663, 866
- Draine B. T., Salpeter E. E., 1979a, *ApJ*, 231, 438
- Draine B. T., Salpeter E. E., 1979b, *ApJ*, 231, 77
- Driver S. P., Popescu C. C., Tuffs R. J., Liske J., Graham A. W., Allen P. D., de Propriis R., 2007, *MNRAS*, 379, 1022
- Duffy A. R., Kay S. T., Battye R. A., Booth C. M., Dalla Vecchia C., Schaye J., 2012, *MNRAS*, 420, 2799
- Dunne L., Eales S., Edmunds M., Ivison R., Alexander P., Clements D. L., 2000, *MNRAS*, 315, 115
- Dunne L., Eales S. A., 2001, *MNRAS*, 327, 697
- Dunne L., Eales S. A., Edmunds M. G., 2003, *MNRAS*, 341, 589
- Dunne L. et al., 2011, *MNRAS*, 417, 1510
- Dwek E., Arendt R. G., 1992, *ARA&A*, 30, 11
- Dwek E., Foster S. M., Vancura O., 1996, *ApJ*, 457, 244
- Eales S. et al., 2009, *ApJ*, 707, 1779
- Eales S. et al., 2010, *PASP*, 122, 499
- Eales S., Lilly S., Gear W., Dunne L., Bond J. R., Hammer F., Le Fèvre O., Crampton D., 1999, *ApJ*, 515, 518
- Edmunds M. G., 2001, *MNRAS*, 328, 223
- Fisher D. B., Bolatto A., Drory N., Combes F., Blitz L., Wong T., 2013, *ApJ*, 764, 174
- Fu J., Kauffmann G., Li C., Guo Q., 2012, *MNRAS*, 424, 2701
- Fukugita M., 2011, *arXiv:1103.4191*
- Fukugita M., Peebles P. J. E., 2004, *ApJ*, 616, 643
- Galametz M., Madden S. C., Galliano F., Hony S., Bendo G. J., Sauvage M., 2011, *A&A*, 532, A56
- Geach J. E., Smail I., Moran S. M., MacArthur L. A., Lagos C. d. P., Edge A. C., 2011, *ApJL*, 730, L19
- Genel S. et al., 2014, *MNRAS*, 445, 175
- Groenewegen M. A. T., 1997, *A&A*, 317, 503
- Hahn O., Abel T., 2011, *MNRAS*, 415, 2101
- Hayward C. C., Jonsson P., Kereš D., Magnelli B., Hernquist L., Cox T. J., 2012, *MNRAS*, 424, 951
- Hayward C. C., Kereš D., Jonsson P., Narayanan D., Cox T. J., Hernquist L., 2011, *ApJ*, 743, 159
- Hayward C. C., Narayanan D., Kereš D., Jonsson P., Hopkins P. F., Cox T. J., Hernquist L., 2013, *MNRAS*, 428, 2529
- Hezaveh Y. D. et al., 2013, *ApJ*, 767, 132
- Hirashita H., 2000, *PASJ*, 52, 585
- Hirashita H., Nozawa T., Villaume A., Srinivasan S., 2015, *MNRAS*, 454, 1620
- Holland W. S. et al., 1999, *MNRAS*, 303, 659

- Hopkins P. F. et al., 2009, *MNRAS*, 397, 802
- Hughes D. H. et al., 1998, *Nature*, 394, 241
- Itoh H., 1989, *PASJ*, 41, 853
- Jones A. P., Tielens A. G. G. M., Hollenbach D. J., McKee C. F., 1994, *ApJ*, 433, 797
- Jonsson P., 2006, *MNRAS*, 372, 2
- Jonsson P., Cox T. J., Primack J. R., Somerville R. S., 2006, *ApJ*, 637, 255
- Karim A. et al., 2011, *ApJ*, 730, 61
- Kennicutt, Jr. R. C. et al., 2009, *ApJ*, 703, 1672
- Knebe A. et al., 2015, *MNRAS*, 451, 4029
- Knudsen K. K., van der Werf P. P., Kneib J.-P., 2008, *MNRAS*, 384, 1611
- Lagache G., Puget J.-L., Dole H., 2005, *ARA&A*, 43, 727
- Lagos C. D. P., Baugh C. M., Lacey C. G., Benson A. J., Kim H.-S., Power C., 2011a, *MNRAS*, 418, 1649
- Lagos C. d. P. et al., 2015, *MNRAS*, 452, 3815
- Lagos C. D. P., Lacey C. G., Baugh C. M., Bower R. G., Benson A. J., 2011b, *MNRAS*, 416, 1566
- Leroy A., Bolatto A., Stanimirovic S., Mizuno N., Israel F., Bot C., 2007, *ApJ*, 658, 1027
- Leroy A. K. et al., 2011, *ApJ*, 737, 12
- Leroy A. K., Walter F., Brinks E., Bigiel F., de Blok W. J. G., Madore B., Thornley M. D., 2008, *AJ*, 136, 2782
- Lo Faro B. et al., 2013, *ApJ*, 762, 108
- Madau P., Dickinson M., 2014, *ARA&A*, 52, 415
- Magdis G. E. et al., 2012, *ApJ*, 760, 6
- Magnelli B. et al., 2012, *A&A*, 539, A155
- Masaki S., Yoshida N., 2012, *MNRAS*, 423, L117
- Mattsson L., Andersen A. C., 2012, *MNRAS*, 423, 38
- Mattsson L., Andersen A. C., Munkhammar J. D., 2012, *MNRAS*, 423, 26
- McGee S. L., Balogh M. L., 2010, *MNRAS*, 405, 2069
- McKinnon R., Torrey P., Vogelsberger M., 2016, *MNRAS*, 457, 3775
- Ménard B., Fukugita M., 2012, *ApJ*, 754, 116
- Ménard B., Scranton R., Fukugita M., Richards G., 2010, *MNRAS*, 405, 1025
- Michałowski M. J., Watson D., Hjorth J., 2010, *ApJ*, 712, 942
- Morokuma-Matsui K., Baba J., 2015, *MNRAS*, 454, 3792
- Muñoz-Mateos J. C. et al., 2009, *ApJ*, 701, 1965
- Narayanan D., Cox T. J., Hayward C. C., Younger J. D., Hernquist L., 2009, *MNRAS*, 400, 1919
- Narayanan D. et al., 2010, *MNRAS*, 407, 1701
- Narayanan D. et al., 2015, *Nature*, 525, 496
- Nozawa T., Kozasa T., Habe A., 2006, *ApJ*, 648, 435
- Nozawa T., Kozasa T., Habe A., Dwek E., Umeda H., Tominaga N., Maeda K., Nomoto K., 2007, *ApJ*, 666, 955
- Obreschkow D., Croton D., De Lucia G., Khochfar S., Rawlings S., 2009, *ApJ*, 698, 1467
- Ostriker J., Silk J., 1973, *ApJL*, 184, L113
- Ouchi M. et al., 2013, *ApJ*, 778, 102
- Planck Collaboration et al., 2014, *A&A*, 571, A16
- Popping G., Caputi K. I., Somerville R. S., Trager S. C., 2012, *MNRAS*, 425, 2386
- Popping G., Somerville R. S., Galametz M., 2016, *arXiv:1609.08622*
- Popping G., Somerville R. S., Trager S. C., 2014, *MNRAS*, 442, 2398
- Reddy N. A., Erb D. K., Pettini M., Steidel C. C., Shapley A. E., 2010, *ApJ*, 712, 1070
- Reddy N. A., Steidel C. C., Fadda D., Yan L., Pettini M., Shapley A. E., Erb D. K., Adelberger K. L., 2006, *ApJ*, 644, 792
- Rémy-Ruyer A. et al., 2014, *A&A*, 563, A31
- Rémy-Ruyer A. et al., 2015, *A&A*, 582, A121
- Riechers D. A. et al., 2013, *Nature*, 496, 329
- Rowlands K. et al., 2012, *MNRAS*, 419, 2545
- Saintonge A. et al., 2011, *MNRAS*, 415, 32
- Salim S. et al., 2007, *ApJS*, 173, 267
- Salpeter E. E., 1977, *ARA&A*, 15, 267
- Santini P. et al., 2014, *A&A*, 562, A30
- Schechter P., 1976, *ApJ*, 203, 297
- Scott S. E. et al., 2002, *MNRAS*, 331, 817
- Sijacki D., Springel V., Di Matteo T., Hernquist L., 2007, *MNRAS*, 380, 877
- Silva L., Granato G. L., Bressan A., Danese L., 1998, *ApJ*, 509, 103
- Skibba R. A. et al., 2011, *ApJ*, 738, 89
- Sklias P. et al., 2014, *A&A*, 561, A149
- Smail I., Ivison R. J., Blain A. W., 1997, *ApJL*, 490, L5
- Smail I., Ivison R. J., Blain A. W., Kneib J.-P., 2002, *MNRAS*, 331, 495
- Smith M. W. L. et al., 2012, *ApJ*, 748, 123
- Smith R. K., Krzewina L. G., Cox D. P., Edgar R. J., Miller, III W. W., 1996, *ApJ*, 473, 864
- Sparre M. et al., 2015, *MNRAS*, 447, 3548
- Sparre M., Springel V., 2016, *MNRAS*, 462, 2418
- Spergel D. N., Flauger R., Hložek R., 2015, *Phys. Rev. D*, 91, 023518
- Springel V., 2010, *MNRAS*, 401, 791
- Springel V., Hernquist L., 2003, *MNRAS*, 339, 289
- Springel V., White S. D. M., Tormen G., Kauffmann G., 2001, *MNRAS*, 328, 726
- Swinbank A. M. et al., 2008, *MNRAS*, 391, 420
- Tacconi L. J. et al., 2008, *ApJ*, 680, 246
- Tacconi L. J. et al., 2013, *ApJ*, 768, 74
- Thacker C. et al., 2013, *ApJ*, 768, 58
- Tielens A. G. G. M., McKee C. F., Seab C. G., Hollenbach D. J., 1994, *ApJ*, 431, 321
- Torrey P., Vogelsberger M., Genel S., Sijacki D., Springel V., Hernquist L., 2014, *MNRAS*, 438, 1985
- Tsai J. C., Mathews W. G., 1995, *ApJ*, 448, 84
- Vieira J. D. et al., 2013, *Nature*, 495, 344
- Vlahakis C., Dunne L., Eales S., 2005, *MNRAS*, 364, 1253
- Vogelsberger M., Genel S., Sijacki D., Torrey P., Springel V., Hernquist L., 2013, *MNRAS*, 436, 3031
- Vogelsberger M. et al., 2014a, *Nature*, 509, 177
- Vogelsberger M. et al., 2014b, *MNRAS*, 444, 1518
- Vogelsberger M., Sijacki D., Kereš D., Springel V., Hernquist L., 2012, *MNRAS*, 425, 3024
- Wang B., Heckman T. M., 1996, *ApJ*, 457, 645
- Watson D., Christensen L., Knudsen K. K., Richard J., Gallazzi A., Michałowski M. J., 2015, *Nature*, 519, 327
- Weiß A. et al., 2013, *ApJ*, 767, 88
- Whitaker K. E., van Dokkum P. G., Brammer G., Franx M., 2012, *ApJL*, 754, L29
- Wiersma R. P. C., Schaye J., Smith B. D., 2009, *MNRAS*, 393, 99
- Wilson G. W. et al., 2008, *MNRAS*, 386, 807
- Winters J. M., Fleischer A. J., Le Bertre T., Sedlmayr E., 1997, *A&A*, 326, 305
- Yahil A., Ostriker J. P., 1973, *ApJ*, 185, 787
- Yajima H., Li Y., Zhu Q., Abel T., 2012, *MNRAS*, 424, 884
- Yasuda Y., Kozasa T., 2012, *ApJ*, 745, 159

Zhukovska S., 2014, A&A, 562, A76
 Zu Y., Weinberg D. H., Davé R., Fardal M., Katz N., Kereš D.,
 Oppenheimer B. D., 2011, MNRAS, 412, 1059

APPENDIX A: ANALYTICAL THERMAL SPUTTERING CALCULATIONS

The empirical thermal sputtering rate given in Equation (1) falls off quickly for $T \lesssim 10^6$ K. In this section, we detail how such a temperature dependence arises from analytical calculations of collisions between gas atoms and grains and the subsequent erosion of grains from sputtering. We refer the reader to the existing literature (Barlow 1978; Draine & Salpeter 1979b; Tielens et al. 1994) for more thorough analysis.

Following Equations 4.19 and 4.20 in Tielens et al. (1994), consider a grain of radius a in a medium of temperature T . Then, the number of particles sputtered off of the grain surface per unit time is given by

$$\frac{dN_{\text{sp}}}{dt} = 2\pi a^2 \sum_i n_i \langle Y_i v \rangle, \quad (\text{A1})$$

where the leading factor of two accounts for collisions at non-normal angles, πa^2 is the grain cross-section, and n_i and $\langle Y_i v \rangle$ are the number density and Maxwell-Boltzmann distribution-averaged product of sputtering yield and velocity for a gas ion of species i . Here, Y_i measures the number of particles sputtered from the grain per gas ion collision (e.g. studied in detail in Section 4.1 of Tielens et al. 1994), and the Maxwell-Boltzmann distribution corresponds to temperature T .

Suppose the grain has mass m and uniform internal density ρ_g and that particles sputtered from the grain surface have mass m_{sp} . For example, a carbonaceous grain might have $m_{\text{sp}} = m_C$, the mass of a carbon atom. The grain mass loss rate

$$\frac{dm}{dt} = 4\pi a^2 \rho_g \frac{da}{dt} \quad (\text{A2})$$

implies that the change in grain radius per unit time due to thermal sputtering is given by

$$\frac{da}{dt} = \frac{n_H m_{\text{sp}}}{2\rho_g} \sum_i A_i \langle Y_i v \rangle, \quad (\text{A3})$$

where A_i is the abundance of gas ions of species i . This sputtering rate is a function of temperature due to its averaging over a Maxwell-Boltzmann distribution. Combined with analytic models of sputtering yields, the thermal sputtering rate shows a sharp drop-off for $T \lesssim 10^6$ K. Thus, the empirical formula given by Equation (1) captures the essential temperature dependence and normalisation of the thermal sputtering rate and avoids the need to calculate Maxwell-Boltzmann distribution-averaged sputtering integrals in our simulation code.

APPENDIX B: VARIATION OF GRAIN SIZE PARAMETER

The fiducial L25n256 run assumed a grain size of $a = 0.1 \mu\text{m}$ to estimate thermal sputtering rates in Equation (2). To investigate the sensitivity of our results to this choice, we performed two additional runs at the same resolution level: one with a smaller grain size ($a = 0.01 \mu\text{m}$) and another with a larger grain size ($a = 1 \mu\text{m}$). Figure B1 shows the cosmic dust density and dust

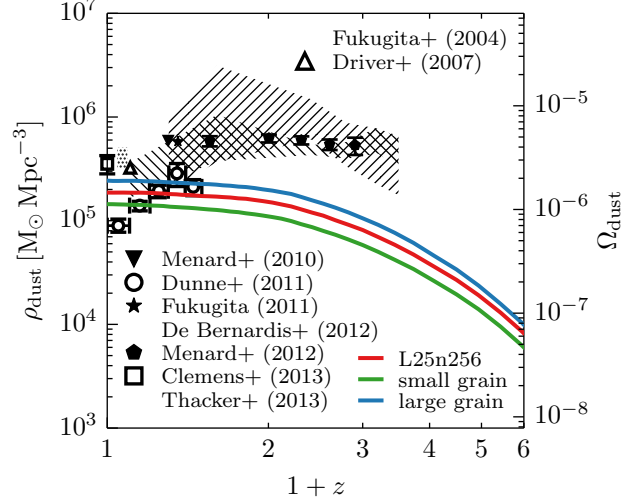


Figure B1. Same as Figure 4, except using the medium-resolution simulation with three grain size parameters. The fiducial L25n256 run uses $a = 0.1 \mu\text{m}$, while the small and large grain runs use $a = 0.01 \mu\text{m}$ and $a = 1 \mu\text{m}$, respectively. Evolution in the cosmic dust density is not sensitive to the choice of grain size parameter.

density parameter for $0 < z < 5$, which was previously studied in Figure 4.

First, the results yield the correct qualitative behaviour: the sputtering time-scale estimated in Equation (2) is longer for larger grains, and we see that by $z = 0$ the cosmic dust density is largest for the $a = 1 \mu\text{m}$ run and smallest for the $a = 0.01 \mu\text{m}$ run. However, the dust densities predicted by these three runs differ by less than a factor of two. Figure 4 demonstrated that change in cosmic dust density when improving resolution from the L25n128 to L25n256 run was just as large as varying the grain size parameter by a factor of 100. Also, the observational data shown for comparison indicate that there are larger uncertainties when estimating the cosmic dust density through a variety of means (e.g. quasar-galaxy reddening correlations, power spectrum measurements, DMF integration, etc.).

Thus, the results presented in Section 3 are not sensitive to our choice of a , especially when considering the combined uncertainties in dust condensation efficiencies, dust mass absorption coefficients, and the amount of dust in galactic haloes.

APPENDIX C: VARIATION OF SIMULATION VOLUME

In addition to the fiducial runs, we also simulate a $(50 h^{-1} \text{Mpc})^3$ volume down to $z = 2.5$ with 2×512^3 dark matter and gas particles to start. This run, labelled L50n512, uses the same fiducial parameters from Table 1 and offers the same spatial and mass resolution as the L25n256 run, but in a volume eight times as large. Figure C1 shows the DMFs for the L25n256 and L50n512 runs at $z = 2.5$, which are nearly identical. The number of galaxies in the mass bin covering $10^{6.5} M_\odot \leq M_{\text{dust}} < 10^{7.0} M_\odot$ has increased from 36 in the L25n256 run to 254 in the L50n512 run, a change similar to the factor of eight increase in volume between these runs. The L50n512 run also forms 10 galaxies in the next highest mass bin, which had no galaxies in the L25n256 run. Figure C1 suggests that the normalisation offset between the simulated DMFs and observations is not the result of limited statistics.

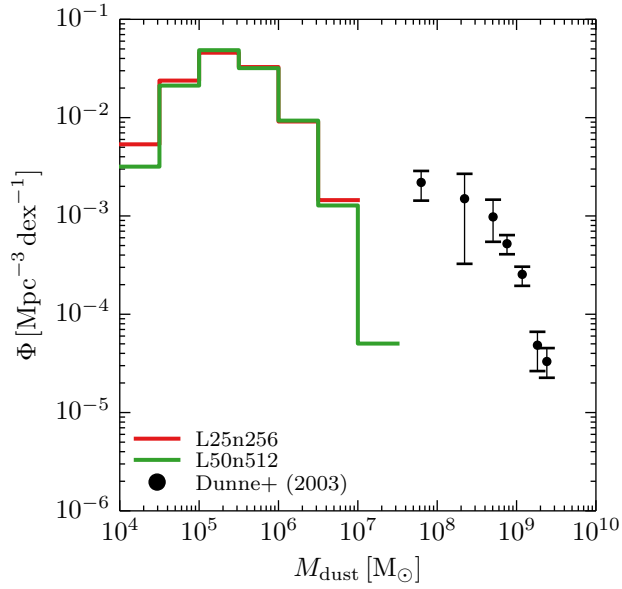


Figure C1. Comparison of the $z = 2.5$ DMFs for the L25n256 run (red) and the L50n512 run (green), the latter of which simulates a $(50 h^{-1} \text{ Mpc})^3$ volume with the same resolution as the L25n256 run. This volume is eight times larger than the fiducial volume and enables us to sample more galaxies. The normalisation of the DMF is not substantially changed by an increase in simulated volume.